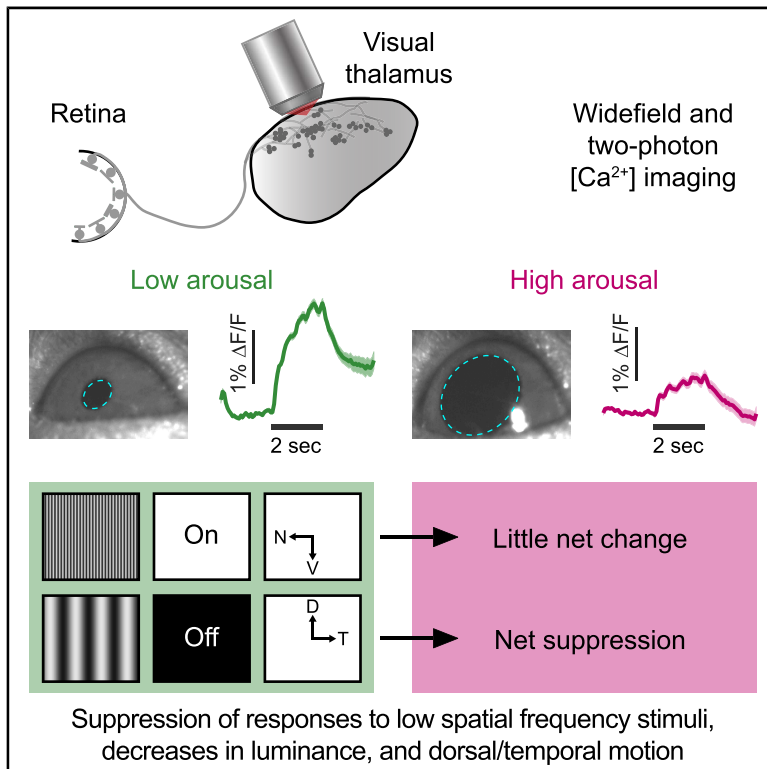


Retinal Inputs to the Thalamus Are Selectively Gated by Arousal

Graphical Abstract



Authors

Liang Liang, Alex Fratzl,
Jasmine D.S. Reggiani,
Omar El Mansour, Chinfei Chen,
Mark L. Andermann

Correspondence

liang.liang@yale.edu (L.L.),
chinfei.chen@childrens.harvard.edu
(C.C.),
manderma@bidmc.harvard.edu (M.L.A.)

In Brief

Using calcium imaging of retinal axonal boutons, Liang et al. reveal differential modulation of distinct visual information channels by arousal state at very early stages of visual processing. Such early filtering may provide an efficient means of optimizing central visual processing and perception across behavioral contexts.

Highlights

- Visual responses of most retinothalamic axonal boutons are suppressed by arousal
- Greater arousal-related suppression of information at lower spatial frequencies
- Greater arousal-related suppression of boutons preferring luminance decrements
- Greater arousal-related suppression of boutons preferring posterior/upward motion



Article

Retinal Inputs to the Thalamus Are Selectively Gated by Arousal

Liang Liang,^{1,2,5,6,*} Alex Fratzl,^{1,3,5,7} Jasmine D.S. Reggiani,^{1,2,4,5} Omar El Mansour,^{1,3} Chinfai Chen,^{2,4,*} and Mark L. Andermann^{1,4,8,*}

¹Division of Endocrinology, Diabetes, and Metabolism, Beth Israel Deaconess Medical Center, Harvard Medical School, Boston, MA 02215, USA

²F.M. Kirby Neurobiology Center, Boston Children's Hospital, Harvard Medical School, Boston, MA 02115, USA

³School of Life Science, École Polytechnique Fédérale de Lausanne (EPFL), Lausanne 1015, Switzerland

⁴Program in Neuroscience, Harvard Medical School, Boston, MA 02115, USA

⁵These authors contributed equally

⁶Present address: Department of Neuroscience, Yale University, New Haven, CT 06510, USA

⁷Present address: Sainsbury Wellcome Centre for Neural Circuits and Behaviour, University College London, London W1T 4JG, UK

⁸Lead Contact

*Correspondence: liang.liang@yale.edu (L.L.), chinfai.chen@childrens.harvard.edu (C.C.), manderma@bidmc.harvard.edu (M.L.A.)

<https://doi.org/10.1016/j.cub.2020.07.065>

SUMMARY

The brain can flexibly filter out sensory information in a manner that depends on behavioral state. In the visual thalamus and cortex, arousal and locomotion are associated with changes in the magnitude of responses to visual stimuli. Here, we asked whether such modulation of visual responses might already occur at an earlier stage in this visual pathway. We measured neural activity of retinal axons using wide-field and two-photon calcium imaging in awake mouse thalamus across arousal states associated with different pupil sizes. Surprisingly, visual responses to drifting gratings in retinal axonal boutons were robustly modulated by arousal level in a manner that varied across stimulus dimensions and across functionally distinct subsets of boutons. At low and intermediate spatial frequencies, the majority of boutons were suppressed by arousal. In contrast, at high spatial frequencies, boutons tuned to regions of visual space ahead of the mouse showed enhancement of responses. Arousal-related modulation also varied with a bouton's preference for luminance changes and direction or axis of motion, with greater response suppression in boutons tuned to luminance decrements versus increments, and in boutons preferring motion along directions or axes of optic flow. Together, our results suggest that differential modulation of distinct visual information channels by arousal state occurs at very early stages of visual processing, before the information is transmitted to neurons in visual thalamus. Such early filtering may provide an efficient means of optimizing central visual processing and perception across behavioral contexts.

INTRODUCTION

Depending on behavioral context, certain sensory stimuli are more relevant than others. Thus, it is beneficial to selectively enhance certain streams of information while suppressing others in a behavioral state-dependent manner. State-dependent modulation of sensory responses has been well-described in sensory cortex [1–13]. In primary visual cortex (V1), locomotion and associated increases in arousal can enhance visually evoked firing rates of orientation-tuned neurons without affecting tuning preferences [2]. Importantly, visual responses are differentially affected by locomotion and/or arousal depending on cell type [2, 10], brain region [10, 11], stimulus attributes [11], and feature preferences [13].

Behavioral modulation also occurs in subcortical sensory areas. In the dorsal lateral geniculate nucleus (dLGN) of the visual thalamus, state-dependent neuromodulation of neuronal resting membrane potential can switch firing patterns from burst to relay mode [14–16]. More recently, locomotion has been correlated

with neuronal response amplitudes in both dLGN and lateral posterior nucleus [17–20]. In dLGN, locomotion differentially enhances responses to sinusoidal gratings at high temporal frequencies, with selective boosting of transient ON neurons and neurons with elevated, nonlinear responses at high spatial frequencies [20]. Such modulation also occurs in a small fraction of superior colliculus neurons [21]. *In vitro* studies suggest that neuromodulatory inputs can already regulate activity at the level of afferent retinal axon terminals [22–25]. However, it remains unclear whether, in the intact animal, brain state selectively modulates information flow at (and / or possibly even before) the level of retinal axons in dLGN.

Recently, we developed methods for simultaneous imaging of visually evoked GCaMP6f calcium responses in hundreds of retinal axonal boutons in dorsal dLGN of awake mice [26]. Here, using pupil area as a metric of arousal [6–8, 12, 27], we compared the response properties of boutons across brain states. Our data revealed that the visual response magnitude of most retinothalamic boutons is strongly suppressed during



arousal, while other boutons are unaffected or enhanced. Surprisingly, the sign and degree of arousal modulation is dependent on the boutons' visual feature preferences (e.g., for motion direction, motion axis, retinotopic location, luminance increases or decreases). We propose that this selective regulation of retinal bouton responses serves to select behaviorally relevant streams of information for additional processing.

RESULTS

Arousal Suppresses Bulk Visual Responses in Retinothalamic Axons

To test whether arousal states modulate visual responses in retinal ganglion cell (RGC) axons projecting to the dLGN, we first conducted widefield calcium imaging in awake, head-fixed mice (Figures 1A and 1B). We presented full-field drifting sinusoidal gratings to the contralateral eye while monitoring pupil area to assess instantaneous arousal levels, similar to previous studies [6–8, 12, 26, 27] (Figure 1C). GCaMP6f-expressing retinal axons were visualized through a cranial window that was chronically implanted over the dLGN and nearby thalamic areas [26] (Figure 1B). The most responsive region within the dLGN was selected as the region of interest (ROI) for quantification. Across individual presentations of the same visual stimulus, the bulk evoked response of RGC axons showed a strong negative correlation with pupil area (Figures 1D and 1E). We defined “low” or “high” arousal trials as those in the lower or upper 25%, respectively, of the pupil area distribution recorded during a given session (Figures 1C, bottom, 1E, shaded regions, and S1A). This corresponded to a ~5-fold larger median pupil area in high versus low arousal trials (Figures S1B and S1C). In the example ROI in Figures 1B–1G, the mean responses to a visual stimulus were ~2-fold smaller in magnitude during high versus low arousal (Figure 1F, spatial frequency: 0.08 cycles per degree [cpd]). To quantify the degree of response modulation, we used a modulation index (MI; $[R_{\text{HighArousal}} - R_{\text{LowArousal}}] / R_{\text{AllTrials}}$; see STAR Methods) for which negative values indicate a suppression of the visual response magnitude during high versus low arousal trials. For the above example, the modulation index was -1.08 . We observed similar suppression of responses to this visual stimulus in all six imaged mice (Figures 1H; 0.08 cpd).

We next examined how this arousal-dependent response suppression varied across grating stimuli spanning four octaves in spatial frequency (0.02, 0.08, 0.32 cpd). In the example ROI, arousal led to response suppression at all spatial frequencies (Figure 1G). Similar results were also observed in five other mice (Figures 1H, S1D, and S1F). Moreover, suppression was significantly greater at low versus high spatial frequencies (0.02 cpd versus 0.32 cpd; Figures 1G, 1H, and S1D).

Additional analyses were performed to rule out alternative explanations for our findings. While pupil area exhibited large fluctuations across tens of seconds (Figures 1C, 1D, and S1A), it might also exhibit slower changes across tens of minutes. If so, response differences between large and small pupil trials could partially reflect slow and systematic changes in responses across a session. However, inspection of pupil areas and response magnitudes from the example session in Figures 1B–1G indicated a negative correlation even when considering consecutive trials (Figure 1D). To quantify this, we estimated modulation indices for pairs of low and high arousal trials spaced

closely or far apart in time. Arousal modulation indices were generally indistinguishable for trials spaced less than 5 min apart versus 15–20 min apart (Figures 2A, 2B, and S2A). Therefore, arousal-dependent response modulation of retinothalamic axonal boutons was correlated with changes in pupil area over both short and longer timescales. We additionally confirmed that the observed arousal-dependent suppression was not related to any cue-evoked changes in pupil diameter, which were either negligibly small or absent (Figure S1E).

Another possible explanation for our results is that horizontal eye movements (while brief relative to our 2 s, full-field stimulus) could cause suppression of neuronal responses, potentially at early visual stages such as the retina [28]. Recent studies suggest that horizontal eye movements in mice are more common during aroused states involving locomotion [1, 2, 12]. Indeed, we observed small ($<5^\circ$) pupil horizontal movements in a subset of high arousal trials, but rarely in low arousal trials (Figure 2C). Thus, we recalculated modulation indices using subsets of high and low arousal trials matched for similar levels of horizontal pupil motion (Figures 2D and 2E) and found them quantitatively similar (Figures 2F and 2G). We also noticed that, in some sessions but not others, the mouse eye appeared to point slightly more ventral ($<10^\circ$ more ventral) during high versus low arousal (Figures S2B–S2D). Similar to the aforementioned analysis, when only considering distributions of high and low arousal trials with matching vertical eye positions (Figure S2E), the results revealed quantitatively similar modulation indices (Figures S2F and S2G). Therefore, the observed arousal-dependent response modulation of retinal axon responses cannot be explained by differences in eye movements or eye position across arousal states.

Arousal-Dependent Response Suppression in Individual Retinothalamic Boutons

Does arousal suppress responses in all retinal axonal boutons or in specific subsets of boutons? To address this question, we recorded simultaneous calcium signals from hundreds of individual retinal boutons in the dLGN “shell” of awake mice using two-photon imaging (Figure 3A; ~20–90 μm below the surface of the dLGN or 80–150 μm below the surface of the optic tract) [26] while monitoring pupil area and running speed to quantify arousal state and locomotion (Figures S3A–S3E). The variability in the magnitude of responses to the same stimulus across trials is illustrated in Figures 3A and 3B for an example direction-selective RGC bouton. Single-trial visual responses were negatively correlated with pupil area—response magnitudes were higher during low versus high arousal states (Figures 3C and 3D). A similar degree of suppression was evident for stimuli presented at the bouton's preferred direction of motion and at all other directions sampled (Figures 3E and S3F). This multiplicative gain change with arousal did not affect direction preference or selectivity for this representative bouton (Figure 3E) or for most other direction-selective boutons (Figures S3G and S3H; cf [2]). Arousal-dependent response suppression was observed in the majority of direction-selective boutons (4,324 boutons from 22 fields of view [FOVs], 5 mice; Figure S3I) when quantifying correlation coefficients and modulation indices (Figures 3F and 3G). State-dependent modulation of visually evoked responses ($\Delta F/F_0$) could not be explained by changes in pre-stimulus baseline

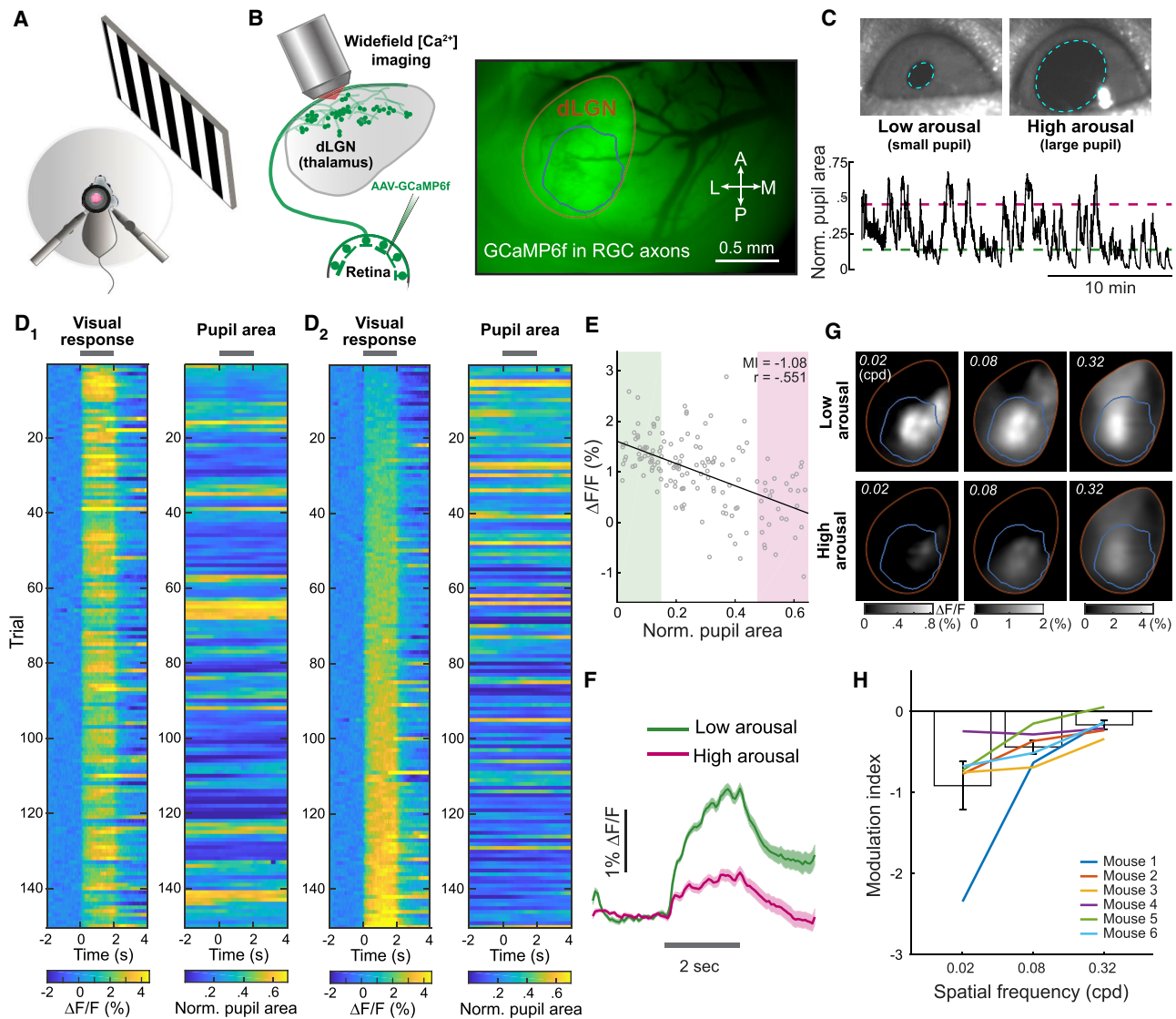


Figure 1. Suppression of Bulk Visual Responses of Retinal Axons in the dLGN during Arousal

(A) Imaging setup.
 (B) Widefield epifluorescence calcium imaging of RGC axons. Left: RGCs were infected with AAV-GCaMP6f. Right: raw fluorescence from retinal axons in the dLGN (orange outline), imaged via a cranial window (bulk activity in D–G estimated from blue subregion). A, anterior; P, posterior; M, medial; L, lateral.
 (C) Arousal levels were estimated by pupil area (top, cyan outline). Bottom: peak-normalized pupil area trace. Magenta and green lines: 75th and 25th percentiles (thresholds for high and low arousal, respectively).
 (D) Time courses of evoked responses to drifting gratings (D₁, left; 0.32 cycles per degree [cpd]) and the corresponding pupil areas (D₁, right), for 150 consecutive trials. Gray bars: stimulus presentation. D₂: same as D₁ but sorted by response amplitude per trial. $\Delta F/F$, fractional change in fluorescence.
 (E) Single-trial responses (drifting gratings: 0.08 cpd) were negatively correlated with pupil area ($r = -0.551$, $p < 10^{-12}$). Green and magenta: low and high arousal regions. MI, modulation index.
 (F) Average response time courses (0.08 cpd) during low (green) and high (magenta) arousal. Mean \pm SEM. Gray line: stimulus presentation.
 (G) Images of average responses during low and high arousal states. Arousal-dependent suppression was stronger for lower spatial frequency stimuli.
 (H). This suppression (negative modulation index) was observed across mice and was strongest at lower spatial frequencies (MIs for 0.02 cpd and 0.32 cpd were significantly different, $p < 0.05$, Friedman test with post hoc Dunn’s test). Mean \pm SEM, N = 6 mice.
 See also [Figure S1](#).

fluorescence, F_0 , which were small and uncorrelated with arousal state (Figures S3J–S3L). Similarly, spontaneous activity during blank trials did not vary with arousal state (Figure S3M).

We previously demonstrated that mouse dLGN neurons in the shell region receive inputs from diverse types of RGCs

that we classified into four broad functional categories: direction-selective (DS; selective to one direction of motion, see above), axis-selective (AS; responsive to opposite directions of motion along the same axis, also known as “orientation-selective”), broadly tuned (BrT; responsive across all directions),

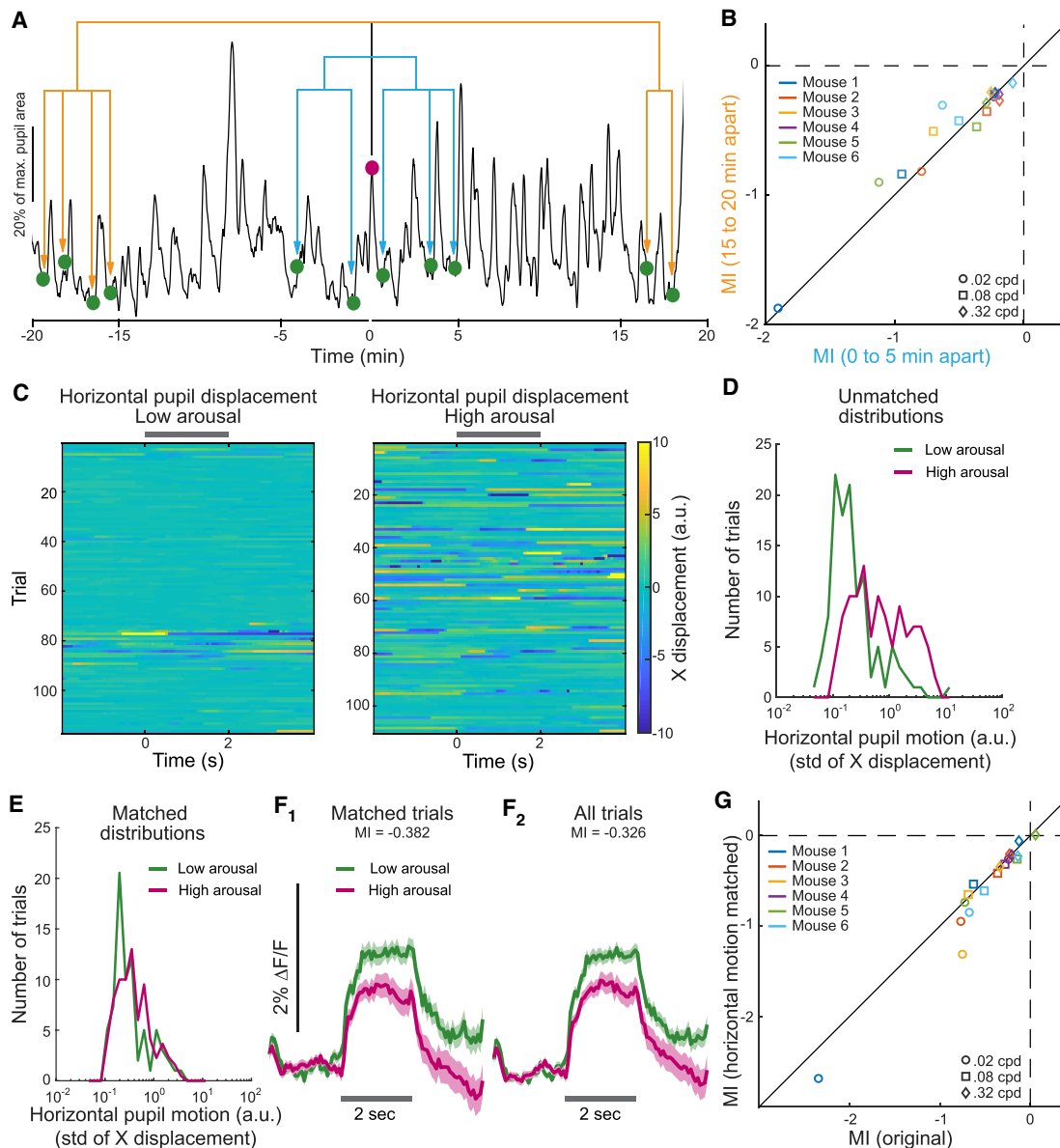


Figure 2. Arousal Modulation Is Not Explained by Slow Changes within a Session or by Pupil Motion

(A) We calculated pairwise MIs between a high arousal trial (magenta) and each low arousal trial (green) within 5 min (blue lines) or spaced 15–20 min apart (orange lines). Black trace: pupil area.

(B) Scatterplot of mean pairwise MI across pairs of high and low arousal trials that were either 0–5 min apart versus 15–20 min apart. Colors: different mice. Symbols: different stimulus spatial frequencies. MIs for nearby or distant pairs of trials were not statistically different at any spatial frequency (two-way repeated-measures ANOVA).

(C) Time courses of horizontal pupil displacement (mean-subtracted, single-trial time course of centroid X position) for all low and high arousal trials (at 0.08 cpd) from one session (see also D–F). Gray bar: stimulus presentation. A.u., arbitrary units.

(D) Distribution of horizontal pupil motion (standard deviation of displacement traces) for low (green) and high (magenta) arousal trials (at 0.08 cpd) in one session.

(E) Distribution of horizontal pupil motion for matched low and high arousal trials from (D) (average across 100 iterations of trial matching; STAR Methods). (F) F_1 : visual responses at 0.08 cpd across arousal states for matched trials. Shown are the mean (across the 100 iterations) of the mean time courses and of the SEMs. F_2 : mean \pm SEM across all trials. Gray line: stimulus presentation.

(G) Scatterplot of MI for all trials (“MI original”) versus horizontal motion-matched subsets of high and low arousal trials (mean MI across iterations). Symbols: see (B). MIs using all versus motion-matched trials were not statistically different at 0.08 cpd or 0.32 cpd (two-way repeated-measures ANOVA; there was a small but significant difference [$p < 0.01$] at 0.02 cpd).

See also Figure S2.

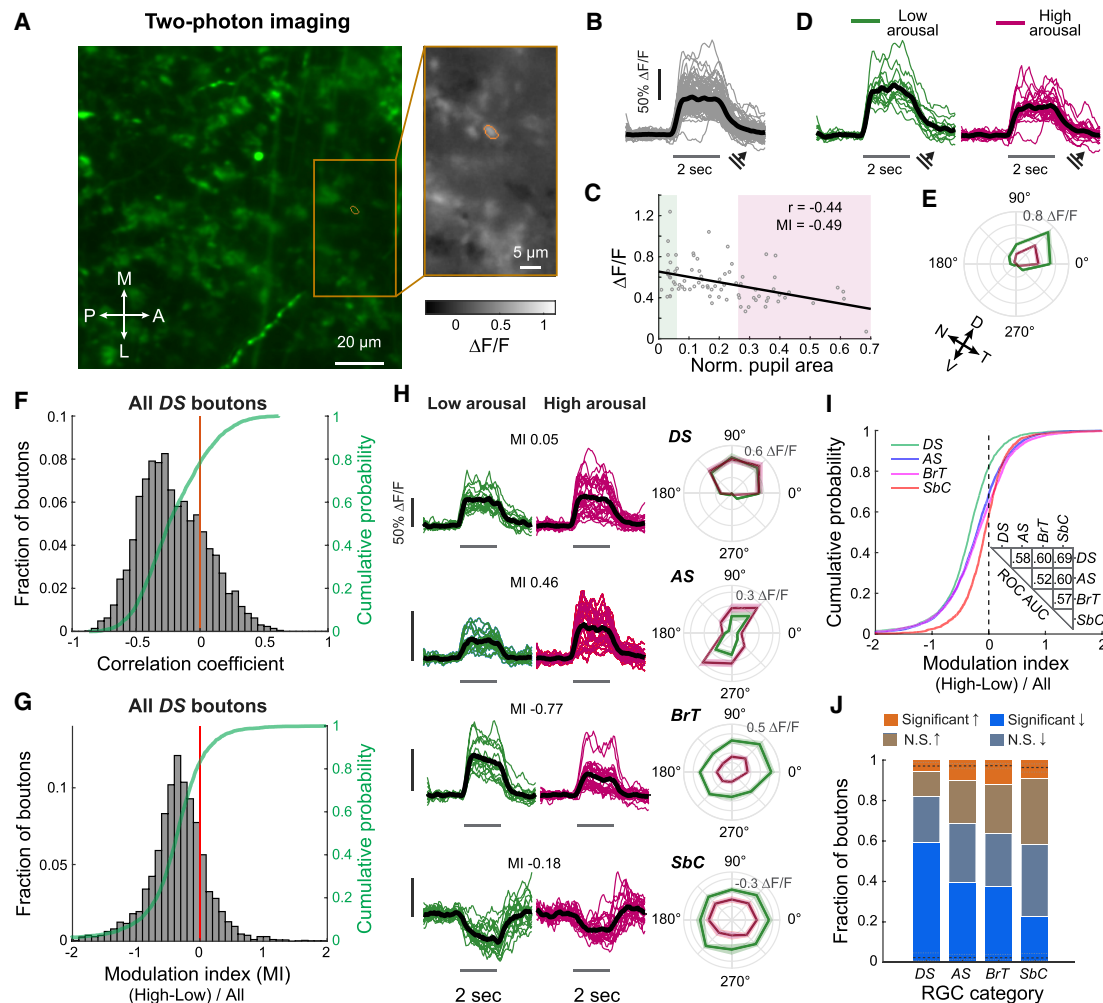


Figure 3. Arousal Suppresses Visual Responses in Individual Retinal Boutons in the dLGN

(A) Left: example raw fluorescence image of retinal axons and axonal boutons in the dLGN, 115 μm below the window. M, medial; L, lateral; A, anterior; P, posterior. Right: average visually evoked calcium responses of RGC boutons from the orange subregion.

(B) Reliable single-trial visual responses of an individual RGC bouton (outlined in A) to presentations of gratings drifting along the bouton's preferred direction (45° , arrow; responses in B–J involve 0.08 cpd gratings).

(C) Single-trial response magnitudes in (B) were negatively correlated with pupil area ($r = -0.44$, $p < 10^{-4}$). Green and magenta indicate low and high arousal states.

(D) Single-trial response time courses (black: means) for this bouton during low or high arousal states.

(E) Direction tuning curves (mean \pm SEM) for this bouton during low or high arousal. 0° : roughly nasal-to-temporal motion on the LCD monitor. 90° : upward motion. Arrows: estimated nasal-temporal (N-T) and dorsal-ventral (D-V) axes, with the head in a typical ambulatory posture.

(F) Visual responses of most direction-selective (DS) boutons (78.3%, 3,386/4,324 boutons from 22 fields of view [FOV], 5 mice) were negatively correlated with arousal. Median correlation: -0.246 . Red line: no correlation. Green: cumulative distribution.

(G) Most DS boutons (82.1%, 2,971/3,619 boutons from 22 FOV, 5 mice) had negative MIs (see STAR Methods; median: -0.336).

(H) Single-trial responses and direction tuning curves across arousal states, from example direction-selective (DS), axis-selective (AS), broadly tuned (BrT), and suppressed-by-contrast (SbC) boutons. The example BrT and SbC boutons were suppressed by arousal, while the example AS bouton was enhanced.

(I) Cumulative distributions of modulation indices for different bouton categories ($N = 3,619$ DS; 3,609 AS; 3,692 BrT; and 1,521 SbC boutons). For DS, AS, BrT, and SbC boutons, 82.1%, 68.6%, 63.6%, and 58.2% of the boutons had negative MI values, respectively. MI distributions differed significantly across pairs of bouton categories (all p values $< 10^{-4}$, Kolmogorov-Smirnov tests with Bonferroni correction). Inset: area under the curve (AUC) for the receiver operating characteristic (ROC) curve for pairs of MI distributions (STAR Methods).

(J) Fraction of boutons per category with significantly enhanced, not significantly (N.S.) enhanced, not significantly suppressed, or significantly suppressed responses. Black dashed lines indicate the median fractions of significantly enhanced or significantly suppressed boutons in shuffled data (1,000 shuffles; gray dashed lines: 95% confidence intervals; STAR methods).

See also Figure S3.

and suppressed-by-contrast (SbC) [26]. Boutons in each category could be significantly enhanced, suppressed, or unaltered by arousal (Figures 3H–3J). Responses of the majority of boutons in each category were significantly suppressed by arousal, most commonly for DS boutons (Figures 3I and 3J), whereas a substantially smaller proportion of boutons was significantly enhanced by arousal (Figure 3J). We wondered whether these results were driven by arousal state *per se* (assessed by pupil area) or by fluctuations in locomotion that often co-vary with pupil size [6, 8, 17, 20]. We confirmed that the observed arousal-dependent modulation effects persisted even when excluding trials involving locomotion (Figures S3A and S3N–S3P).

Arousal-Related Response Modulation Varies across Spatial Frequencies

Consistent with our bulk imaging results (Figure 1), arousal-dependent suppression was greater for low versus high spatial frequency stimuli across populations of retinal boutons (Figure 4A). Accordingly, for low and intermediate spatial frequency stimuli, many boutons showed significant arousal-related response suppression, whereas a smaller proportion showed significant response enhancement (Figure 4B). These results were consistent across individual mice (averaging across all sessions per mouse) and across individual sessions (Figures 4C and S4A).

Arousal-Related Response Suppression Depends on Retinotopic Preference

Our findings show arousal-dependent response modulation of retinthalamic boutons depends on stimulus spatial frequency. However, even when separately considering each spatial frequency, we observed substantial heterogeneity in modulation across boutons in each broad RGC category (Figures 3I and 3J). Thus, we wondered whether a bouton's arousal-dependent modulation also varied with other tuning properties. We estimated each bouton's retinotopic preference by presenting elongated bars containing spatiotemporal noise (Figures 4D and 4E; [26]). We then mapped each bouton's arousal modulation index onto its retinotopic preference in azimuth and elevation, creating a spatial map of arousal modulation for each stimulus spatial frequency (Figure 4F). At the lowest spatial frequency used (0.02 cpd), grating responses were suppressed by arousal in most boutons, regardless of their preferred retinotopic location. However, this map became more spatially heterogeneous at the highest spatial frequency used (0.32 cpd). In this case, arousal actually enhanced responses to drifting gratings for boutons tuned to stimuli in dorsal and nasal regions of visual space (see Region 1, Figures 4F and 4G, right, and S4B, right) while suppressing responses in boutons tuned to other regions of space. This heterogeneity in arousal modulation by retinotopic preference contributed to the variability in arousal modulation that we observed across mice and sessions (Figure 4C), as recordings in different mice and sessions were often focused on boutons preferring different regions of visual space (Figure S4C). The maps of modulation index relative to boutons' retinotopic preferences were similar when the four broad bouton categories were considered separately (Figures S4D–S4G).

Greater Arousal-Related Response Suppression in “Off” versus “On” Retinal Boutons

We next considered the relationship between arousal modulation and a bouton's response tuning to full-field changes in luminance. We classified RGC boutons as either “On” type (selective to luminance increases), “Off” type (selective to luminance decreases), or “On-Off” type (responsive to both) (Figures 5A and 5B). We estimated the arousal modulation index for each bouton's responses to full-field drifting gratings, as above (Figure 5A). Similar numbers of On boutons were enhanced or suppressed by arousal, whereas ~80% of Off boutons were suppressed by arousal. The distribution of modulation index values differed significantly between On and Off boutons (Figures 5C and 5D). Similar differences in arousal modulation of On versus Off boutons were evident when we separately considered each broad RGC category (Figures S5A and S5B) and each stimulus spatial frequency (Figures S5C–S5F).

Arousal-Dependent Response Suppression Depends on Direction and Axis Preference

The significance of visual motion along different directions or axes might change depending on behavioral state. In an unaroused and stationary mouse, detection of any motion may be essential to respond to approaching predators or threats. In contrast, for an aroused mouse that is moving forward, visual motion signals include self-generated optic flow signals, which may be less relevant. We thus considered arousal modulation of responses to moving gratings in two non-overlapping categories of motion-selective retinal boutons—DS or AS boutons. We previously showed that the dLGN subregion that we imaged contains DS boutons preferring one of four directions of motion. The majority of these DS boutons prefer posterior or upward motion in visual space ([26]; Figure 6A₁). While boutons tuned to all four directions showed arousal-dependent suppression on average, suppression was larger and more common for boutons preferring posterior or upward motion (Figures 6A₂–6A₄ and S6A). This directional bias in arousal modulation may serve to attenuate self-generated visual signals related to optic flow, which is anticipated during current or upcoming locomotion, while preserving encoding of other motion that might indicate movement of animate objects. We also repeated analyses restricted to trials in which mice were stationary and confirmed that elevated arousal modulates retinal processing in a direction-specific manner even in the absence of locomotion (Figure S6B). A similar directional bias in the degree of arousal modulation was observed across a range of spatial frequencies (0.02–0.32 cpd; Figures S6C and S6D).

We also analyzed AS boutons tuned to motion along a specific axis. AS boutons preferring horizontal motion were more commonly suppressed than AS boutons preferring vertical motion (Figures 6B and S6E). This finding persisted when only considering stationary trials (Figure S6F) and was also consistent across other stimulus spatial frequencies (Figures S6G and S6H).

DISCUSSION

We demonstrated that visual response magnitudes differ across arousal states at a very early stage in the image-forming

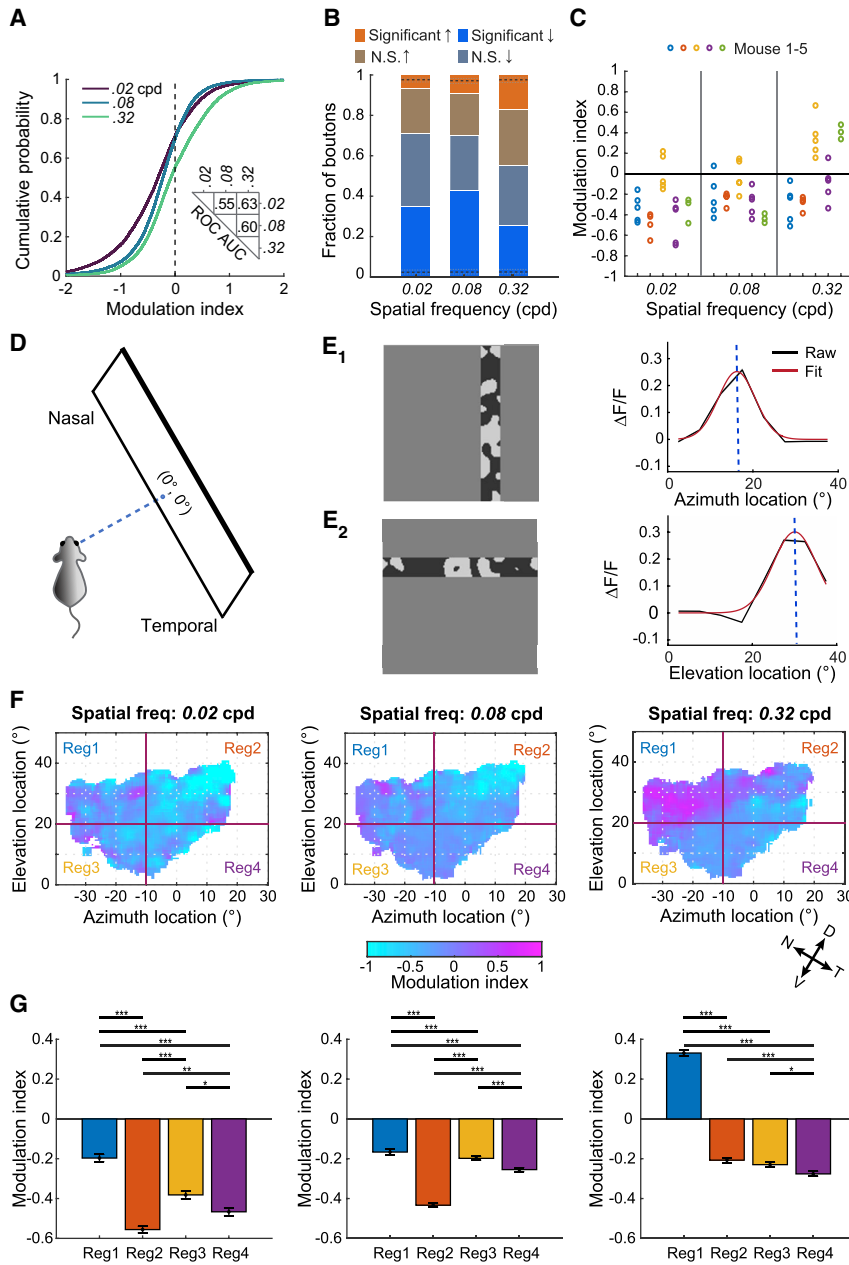


Figure 4. Differential Arousal Modulation of Boutons across Spatial Frequencies and Retinotopic Locations

(A) Cumulative distributions of modulation indices for different spatial frequencies, pooled across bouton categories (N = 8,074, 12,441, and 11,311 boutons with significant responses at 0.02, 0.08 and 0.32 cpd, respectively). 71.0%, 69.8%, and 55.3% of the boutons had negative MI values, respectively. Distributions were all significantly different from each other (all p values < 10⁻⁶³, Kolmogorov-Smirnov tests with Bonferroni correction). Inset: ROC AUC between pairs of distributions.

(B) Fraction of boutons driven at a given spatial frequency that were significantly enhanced, not significantly (N.S.) enhanced, not significantly suppressed, or significantly suppressed. Black dashed lines indicate the median fractions of boutons that were significantly enhanced or significantly suppressed in shuffled data (1,000 shuffles; gray dashed lines: 95% confidence intervals).

(C) Average MI across all boutons recorded in a session, plotted for each session and stimulus spatial frequency. Sessions from the same mouse have the same color. We found significant effects of spatial frequency (p < 10⁻⁴), mouse (p < 10⁻⁴), the interaction of these two (p < 10⁻⁴), and session (p = 0.02) (two-way repeated-measures ANOVA). Tukey's multiple comparisons test: 0.02 versus 0.08 cpd, N.S.; 0.02 versus 0.32 cpd, p < 0.001; 0.08 versus 0.32 cpd, p < 0.05.

(D) Schematic of the relative location of the monitor and the eye contralateral to the imaged hemisphere. The intersection point where a perpendicular dashed line from the mouse face meets the monitor was designated as 0° in azimuth and 0° in elevation.

(E) E₁, left: retinotopic mapping of azimuth involved spatiotemporal noise within a vertical bar, presented randomly at different horizontal locations (5° spacing). Right: retinotopic response tuning curve (black) and model fit (red) for one individual bouton. E₂: same as E₁ but for mapping of elevation.

(F) Modulation indices of individual boutons mapped to their preferred retinotopic locations in visual space. The map for each spatial frequency includes all DS, AS, BrT, and SbC boutons. Maps were smoothed using a 3° window. Portions of the maps for which no recorded boutons with corresponding retinotopic preferences exist are shown in white. We compared MI distributions across regions by dividing each map into four regions (red lines; see below). Estimates of elevation

and azimuth are in LCD monitor coordinates (see D). Arrows at bottom right indicate rough estimates of natural axes of elevation and azimuth during typical ambulatory posture [29].

(G) Average arousal modulation index of the four regions for each spatial frequency. Mean ± SEM. Number of boutons for the four regions at 0.02 cpd: 1,235, 1,872, 1,058, and 1,038; at 0.08 cpd: 1,908, 3,005, 1,730, and 1,673; and at 0.32 cpd: 1,654, 2,325, 1,566, and 1,433. For each spatial frequency, distributions of indices were significantly different across regions (Kruskal-Wallis test, all p values < 10⁻⁵⁰, post hoc Dunn's multiple comparison test: *p < 0.05; **p < 0.01; ***p < 0.001).

See also Figure S4.

pathway—before information is transmitted to the visual thalamus. Surprisingly, visually evoked activity in the majority of retinal boutons was suppressed during arousal. This suppression was the prevailing effect in both widefield and two-photon calcium imaging data. Moreover, the degree of suppression depended on the spatial frequency of the stimulus, with stronger

suppression of responses to lower spatial frequency stimuli. Although responses in the majority of boutons were suppressed by arousal, responses of some boutons were enhanced, particularly to higher spatial frequency stimuli and stimuli located in nasal and dorsal regions of visual space. Such heterogeneity was evident across all four broadly defined functional categories

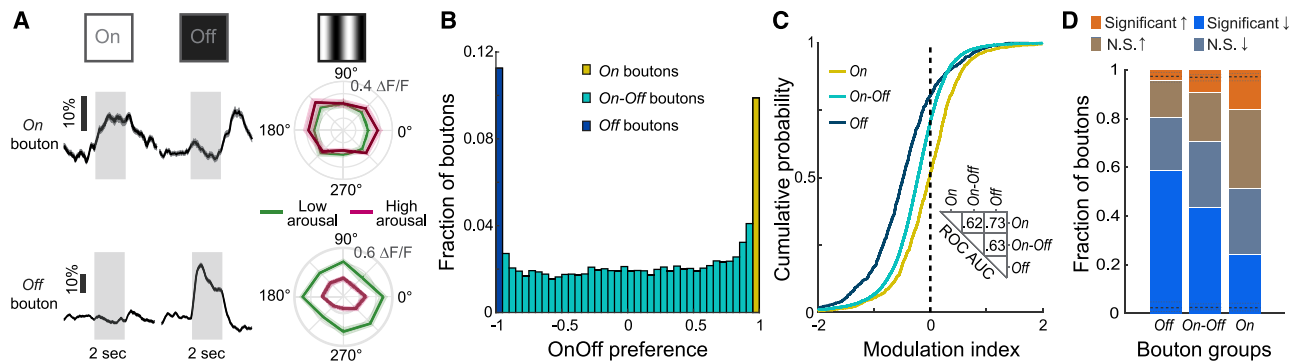


Figure 5. Greater Arousal-Related Response Suppression in Off versus On Retinal Boutons

(A) Average response time courses during full-field luminance increments (left) and decrements (middle), and direction tuning curves of average responses to full-field drifting gratings (right), from an example On bouton and an example Off bouton. Mean \pm SEM.

(B) Fraction of boutons defined as “On” (OnOff preference index >0.95 , $N = 1364$), “Off” (index < -0.95 , $N = 1553$), or “On-Off” (index within $[-0.95, 0.95]$, $N = 10877$). Data from 22 FOV from 5 mice.

(C) Cumulative distributions of modulation indices (for 0.08 cpd stimuli) for On, On-Off, and Off boutons. Distributions were all significantly different from each other (all p values $< 10^{-34}$, Kolmogorov-Smirnov tests with Bonferroni correction). 51.5%, 70.6%, and 80.5% of On, On-Off, and Off boutons had negative index values, respectively. Inset: ROC AUC between pairs of distributions.

(D) Fraction of boutons of each type with significantly enhanced, not significantly (N.S.) enhanced, not significantly suppressed, or significantly suppressed responses (to 0.08 cpd stimuli). Black dashed lines indicate the median fraction of boutons that were significantly enhanced or significantly suppressed in shuffled data (1,000 shuffles; gray dashed lines: 95% confidence intervals).

See also Figure S5.

of RGCs: direction-tuned, axis-tuned, broadly tuned, and suppressed. We also classified boutons according to preferences for luminance changes. We found that On boutons showed equal likelihood of arousal-related enhancement or suppression, while Off boutons were mostly suppressed by arousal. For the region of visual space that we examined, arousal modulation also depended on the bouton’s preferred motion direction and motion axis, with greater suppression in boutons tuned to directions of optic flow. Taken together, these findings indicate differential modulation of distinct visual information channels prior to the stage of processing by thalamic neurons.

Selective Transmission of Retinal Information across Arousal States

Brain state-dependent visual processing in rodents has been studied in visual cortical neurons [1–3, 8–13, 30, 31] and in dLGN neurons [17, 19, 20]. A number of these studies have demonstrated heterogeneity in modulation by locomotion [10, 13, 17, 20]. Our findings showing selective, arousal-related response suppression at the level of retinal axon terminals may reflect an efficient means of filtering out less relevant information before it gets amplified by thalamocortical circuits. Indeed, our results are consistent with the findings of Aydin et al. [20], showing preferential locomotion-related enhancement of transient On dLGN neurons and a subset of neurons tuned to high spatial frequencies. Suppression of distinct information streams at an early stage of visual processing could serve several purposes. First, as described above, the suppression of visual signals related to optic flow may allow more efficient coding of unexpected signals such as those from moving objects in the environment. Second, an increase in arousal may warrant a shift in visual processing from detection of possible threats to high-resolution discrimination of bright objects in front of the animal. A parallel change in optimization

for detection or discrimination has been suggested for downstream dLGN neurons during low arousal (burst mode firing) or high arousal (tonic mode firing), respectively [32].

Previous studies have considered either pupil area or changes in pupil area as indicators of arousal [6–8, 12]. While additional insights might be gained by considering both pupil area and its temporal derivative, we chose the former because early analyses of raw data from individual boutons (e.g., Figure 3C) and bulk recordings (e.g., Figures 1E and S1F) showed a roughly linear relationship between pupil area and response magnitude. Note that the pupil diameters typically observed in our study (Figure S3E) correspond to a range for which auditory cortical excitability and behavioral sensitivity monotonically increase with increasing pupil diameter [6].

Potential Mechanisms Underlying Arousal Dependence of Responses in Retinal Boutons

Arousal-related response suppression at the level of RGC axons could be due to a combination of several mechanisms. As discussed below, these include direct neuromodulation of RGC axons in the dLGN, modulation of retinal responses by retinopetal brainstem projections, and/or changes in luminance due to variations in pupil area. While a dissection of these possible mechanisms is beyond the scope of this study, it is worthwhile considering them in greater detail (see also [33]). First, a number of neuromodulators are known to act on RGC axon terminals in dLGN and elsewhere to inhibit presynaptic calcium influx and neurotransmitter release [22–25, 34]. GABA_B receptors could mediate direct inhibition of RGC axon terminals by thalamic reticular neurons and/or local inhibitory neurons, both of which receive top-down input from cortex and elsewhere [15, 35]. Interestingly, while serotonin has been shown to inhibit retinothalamic transmission by activation of 5HT-1B receptors [23], it can enhance excitability of postsynaptic thalamocortical neurons

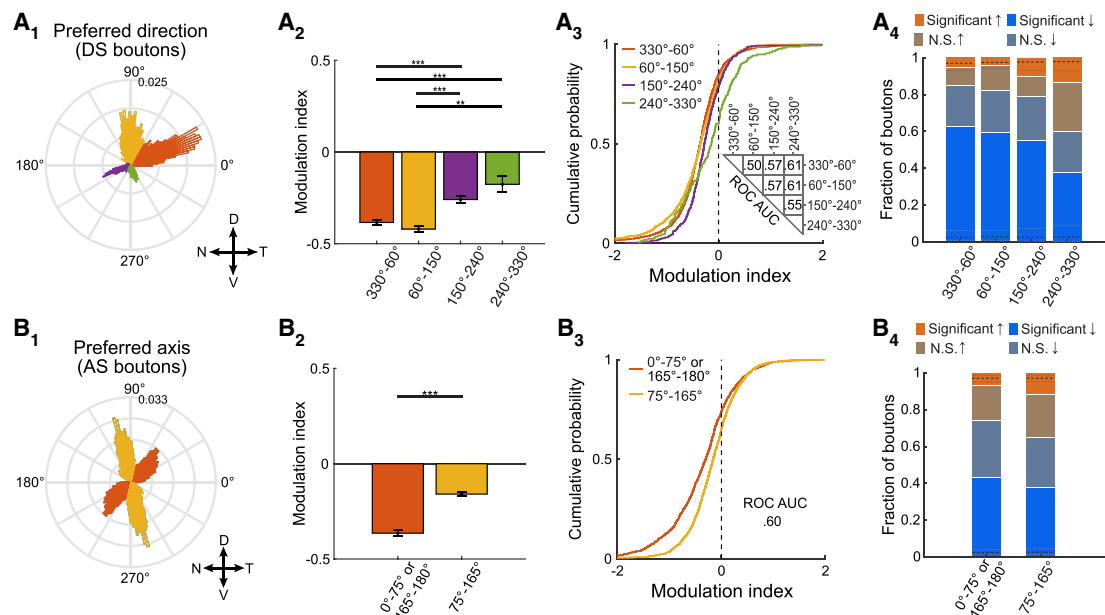


Figure 6. Differential Arousal Modulation of Boutons with Distinct Motion Preferences

(A) A₁, the distribution of motion direction preferences across direction-selective (DS) boutons had four distinct peaks. Accordingly, we manually defined four groups of DS boutons (distinct colors). Ns for groups of boutons with direction preferences between 330°–60°, 60°–150°, 150°–240°, and 240°–330° were 1,924, 1,143, 372, and 180, respectively. Data from 22 FOV from 5 mice. A₂, average arousal modulation index of DS boutons in each group. Mean ± SEM. Distributions of indices were significantly different across groups (Kruskal-Wallis test, $p < 10^{-8}$, post hoc Dunn’s multiple comparison test: ** $p < 0.01$; *** $p < 0.001$). A₃, cumulative distributions of modulation indices for the four groups. Indices were negative for 84.8%, 82.1%, 78.8%, and 60.0% of boutons. All pairs of distributions were significantly different (150°–240° versus 240°–330°: $p = 0.0015$; all other comparisons: $p < 10^{-3}$; Kolmogorov-Smirnov tests with Bonferroni correction), except for 330°–60° versus 60°–150° ($p = 0.10$). Inset: ROC AUC between pairs of distributions. A₄, Fraction of boutons per group with significantly enhanced, not significantly (N.S.) enhanced, not significantly suppressed, or significantly suppressed responses (at 0.08 cpd). Black dashed lines indicate median fractions of boutons that were significantly enhanced or significantly suppressed in shuffled data (across 1,000 shuffles; gray dashed lines: 95% confidence intervals). D, dorsal; V, ventral; N, nasal T, temporal. Note that polar axes have been rotated by 31° such that 0° indicates nasal-to-temporal motion during typical ambulatory posture [29].

(B) B₁, the distribution of motion axis preferences across AS boutons had two distinct peaks. Accordingly, we manually defined two groups of AS boutons (distinct colors). Ns for groups of boutons with preferences ranging from 0°–75° or 165°–180° and 75°–165° were 1,402 and 2,207, respectively. Note that the orange group spanning the union of 0°–75° and 165°–180° is equivalent to spanning from –15° to 75°, as axis preferences of –180°–0° mirror that of 0°–180°. Data from 22 FOV from 5 mice. B₂, average arousal modulation index of AS boutons in each group. Mean ± SEM. Medians of the two distributions were significantly different (** $p < 10^{-22}$, Wilcoxon rank sum test). B₃, cumulative distributions of modulation indices for each group. Indices were negative for 74.0% and 65.1% of boutons. Distributions were significantly different ($p < 10^{-22}$, Kolmogorov-Smirnov test). Inset: ROC AUC between the two distributions. B₄, Fraction of boutons per group with significantly enhanced, not significantly (N.S.) enhanced, not significantly suppressed, or significantly suppressed responses (at 0.08 cpd). Black dashed lines indicate median fractions of boutons that were significantly enhanced or significantly suppressed in shuffled data (1,000 shuffles).

See also Figure S6.

[36, 37]. This opposing modulation may serve to suppress less relevant signals at the RGC bouton, thus allowing pertinent information to be efficiently transmitted to the dLGN and amplified in downstream circuits. In addition to these known actions on RGC axon terminals, neuromodulatory retinopetal projections may also act directly on RGC cell bodies [38].

The increase in pupil diameter during arousal may also contribute to the observed response suppression, due to the associated increase in overall retinal illumination. We observed a ~5-fold increase in median pupil area in high versus low arousal states. Thus, arousal could cause a similar increase in retinal illumination, though this increase may be partially mitigated by increased absorbance of incident light via a concomitant increase in retinal blood flow and volume. Several studies demonstrate that larger changes in illuminance (i.e., orders of magnitude increases) within a similar luminance range (scotopic to mesopic) can modify mouse retinal processing [39–41]. However, the phenomena described in these studies cannot account

for many of our results. First, Farrow et al. [39] show an abrupt step-change in inhibition of certain RGC types beyond a certain threshold luminance level. In contrast, our findings indicate that the change in response magnitude is roughly linear across the entire range of pupil areas (e.g., Figures 1E, 3C, and S1F). Second, it is not clear that luminance alone can explain the feature specificity of the arousal modulation that we observed. Notably, we show that RGC boutons can be differentially modulated based on their preferred direction of motion. Likewise, luminance effects on RGC activity might be expected to be generally consistent across the retina, whereas we show that RGC boutons encoding nasal or dorsal versus temporal or ventral aspects of visual space differ in their typical magnitude and sign of arousal modulation. Additionally, while arousal typically suppresses visual responses in retinal axonal boutons in both the dLGN and superior colliculus [33], aspects of arousal modulation differ markedly between these two target areas. For example, arousal differentially modulates responses of retinal boutons in

the dLGN depending on their preferences for motion direction or motion axis (Figure 6) or On or Off preferences (Figure 5). This selective modulation of functional subsets of retinal boutons by arousal was not evident in the superior colliculus [33]. These data further suggest that, while changes in retinal illumination may contribute to some of our findings, local neuromodulation at the level of each retinal target area also shapes the effects of arousal on retinal axonal bouton responses.

The diversity of bouton sensitivities to arousal, together with the lack of changes in baseline fluorescence across states, also argue against a major contribution from arousal-related changes in thalamic blood flow to our data. As discussed above, we also ruled out major contributions from changes in eye movement or eye position with arousal. An increased pupil area might also drive the observed effects via a decreased depth of field [42]. However, this would lead to blurring of stimuli that are presented outside the focal plane, particularly stimuli with higher spatial-frequency content. In contrast, we observed larger arousal-dependent suppression of responses for stimuli at lower spatial frequencies.

How might future studies directly assess whether arousal modulation of retinal axonal boutons occurs presynaptically in the dLGN or whether similar modulation is already present in the retina? One strategy for assessing effects of illumination involves direct dilation of the pupil(s) [17, 43]. However, this strategy can cause compensatory squinting at the luminance levels used in this study (data not shown). Arousal modulation of presynaptic axon terminals could be assessed by bypassing retinal transduction via direct electrical stimulation of the optic tract (see [44] for a similar strategy applied to the whisker somatosensory system). Indeed, pairing of optic nerve electrical stimulation with stimulation of dorsal raphe neurons *in vivo* was shown to suppress electrically evoked responses in thalamocortical cells in dLGN [45, 46].

Implications for Thalamocortical Coding of the Visual World

Regardless of the potential mechanisms involved, our findings demonstrate that arousal can influence the nature and magnitude of visual information transmission from a very early stage in the image-forming pathway. Somehow, the central visual system must make sense of the visual world despite these major differences in information received from RGC axons across arousal states.

Behavioral states play important roles in shaping neural dynamics, sensory perception, and behavior performance. This has led to a surge of studies evaluating state-dependent modulation of visual responses in thalamic and cortical neurons. Our findings highlight the existence of flexible, feature-specific gating of visual responses at even earlier stages of this pathway, providing a powerful, efficient, and state-dependent means for exclusion of less relevant information by the early visual system.

STAR★METHODS

Detailed methods are provided in the online version of this paper and include the following:

- KEY RESOURCES TABLE
- RESOURCE AVAILABILITY
 - Lead Contact
 - Materials Availability

- Data and Code Availability
- EXPERIMENTAL MODEL AND SUBJECT DETAILS
- METHOD DETAILS
 - Viral injection
 - Headpost and cranial window implantation
 - Epifluorescence and two-photon calcium imaging
 - Pupil videography and image analysis
 - Locomotion during two-photon imaging
 - Visual Stimulation
 - Image processing
 - Estimation of visual tuning preferences in RGC boutons
 - Bouton type classification
 - Arousal modulation
 - Arousal modulation during the stationary state
 - Trial matching
 - Estimation of retinotopic preferences in RGC boutons
- QUANTIFICATION AND STATISTICAL ANALYSES

SUPPLEMENTAL INFORMATION

Supplemental Information can be found online at <https://doi.org/10.1016/j.cub.2020.07.065>.

ACKNOWLEDGMENTS

We thank members of the Andermann and Chen labs for helpful discussion. We thank Drs. Jayaraman, Kerr, Kim, Looger, and Svoboda and the GENIE Project, Janelia Farm Research Campus, HHMI, for GCaMP6. We thank the Boston Children's Hospital viral core for virus packaging. Support was provided by a Simons Collaboration on the Global Brain Postdoctoral Fellowship and a Klingenstein-Simons Fellowship (to L.L.); a Bertarelli Foundation Fellowship (to A.F.); NIH (R01EY013613 to C.C.); the Harvard/MIT Joint Research Grants Program in Basic Neuroscience and NIH R21 EY030243 (to C.C. and M.L.A.); NIH DP2DK105570, R01 DK109930, DP1 AT010971 and grants from the Smith Family Foundation, the Pew Scholars Program in the Biomedical Sciences, and the Klarman Family Foundation (to M.L.A.); the IDDR Cellular Imaging Core (supported by U54 HD090255), and the BCH Viral Core (supported by NIH P30 EY012196).

AUTHOR CONTRIBUTIONS

L.L., A.F., C.C., and M.L.A. conceived and designed the study. L.L. and J.D.S.R. performed surgeries and imaging experiments. L.L., A.F., J.D.S.R., and O.E.M. analyzed the data. L.L., J.D.S.R., A.F., C.C., and M.L.A. wrote the manuscript with input from all authors.

DECLARATION OF INTERESTS

The authors declare no competing interests.

Received: March 14, 2020
 Revised: June 12, 2020
 Accepted: July 21, 2020
 Published: August 13, 2020

REFERENCES

1. Bennett, C., Arroyo, S., and Hestrin, S. (2013). Subthreshold mechanisms underlying state-dependent modulation of visual responses. *Neuron* 80, 350–357.
2. Niell, C.M., and Stryker, M.P. (2010). Modulation of visual responses by behavioral state in mouse visual cortex. *Neuron* 65, 472–479.

3. Polack, P.-O., Friedman, J., and Golshani, P. (2013). Cellular mechanisms of brain state-dependent gain modulation in visual cortex. *Nat. Neurosci.* *16*, 1331–1339.
4. Schneider, D.M., Nelson, A., and Mooney, R. (2014). A synaptic and circuit basis for corollary discharge in the auditory cortex. *Nature* *513*, 189–194.
5. Zhou, M., Liang, F., Xiong, X.R., Li, L., Li, H., Xiao, Z., Tao, H.W., and Zhang, L.I. (2014). Scaling down of balanced excitation and inhibition by active behavioral states in auditory cortex. *Nat. Neurosci.* *17*, 841–850.
6. McGinley, M.J., David, S.V., and McCormick, D.A. (2015). Cortical Membrane Potential Signature of Optimal States for Sensory Signal Detection. *Neuron* *87*, 179–192.
7. McGinley, M.J., Vinck, M., Reimer, J., Batista-Brito, R., Zagha, E., Cadwell, C.R., Tolia, A.S., Cardin, J.A., and McCormick, D.A. (2015). Waking State: Rapid Variations Modulate Neural and Behavioral Responses. *Neuron* *87*, 1143–1161.
8. Vinck, M., Batista-Brito, R., Knoblich, U., and Cardin, J.A. (2015). Arousal and locomotion make distinct contributions to cortical activity patterns and visual encoding. *Neuron* *86*, 740–754.
9. Stringer, C., Pachitariu, M., Steinmetz, N., Reddy, C.B., Carandini, M., and Harris, K.D. (2019). Spontaneous behaviors drive multidimensional, brain-wide activity. *Science* *364*, eaav7893.
10. Dipoppa, M., Ranson, A., Krumin, M., Pachitariu, M., Carandini, M., and Harris, K.D. (2018). Vision and Locomotion Shape the Interactions between Neuron Types in Mouse Visual Cortex. *Neuron* *98*, 602–615.
11. Andermann, M.L., Kerlin, A.M., Roumis, D.K., Glickfeld, L.L., and Reid, R.C. (2011). Functional specialization of mouse higher visual cortical areas. *Neuron* *72*, 1025–1039.
12. Reimer, J., Froudarakis, E., Cadwell, C.R., Yatsenko, D., Denfield, G.H., and Tolia, A.S. (2014). Pupil fluctuations track fast switching of cortical states during quiet wakefulness. *Neuron* *84*, 355–362.
13. Mineault, P.J., Tring, E., Trachtenberg, J.T., and Ringach, D.L. (2016). Enhanced Spatial Resolution During Locomotion and Heightened Attention in Mouse Primary Visual Cortex. *J. Neurosci.* *36*, 6382–6392.
14. McCormick, D.A., and Bal, T. (1997). Sleep and arousal: thalamocortical mechanisms. *Annu. Rev. Neurosci.* *20*, 185–215.
15. McCormick, D.A. (1992). Neurotransmitter actions in the thalamus and cerebral cortex and their role in neuromodulation of thalamocortical activity. *Prog. Neurobiol.* *39*, 337–388.
16. Sherman, S.M., and Guillery, R.W. (2001). *Exploring the Thalamus* (California: Academic Press).
17. Erisken, S., Vaiceliunaite, A., Jurjut, O., Fiorini, M., Katzner, S., and Busse, L. (2014). Effects of locomotion extend throughout the mouse early visual system. *Curr. Biol.* *24*, 2899–2907.
18. Roth, M.M., Dahmen, J.C., Muir, D.R., Imhof, F., Martini, F.J., and Hofer, S.B. (2016). Thalamic nuclei convey diverse contextual information to layer 1 of visual cortex. *Nat. Neurosci.* *19*, 299–307.
19. Williamson, R.S., Hancock, K.E., Shinn-Cunningham, B.G., and Polley, D.B. (2015). Locomotion and Task Demands Differentially Modulate Thalamic Audiovisual Processing during Active Search. *Curr. Biol.* *25*, 1885–1891.
20. Aydin, Ç., Couto, J., Giugliano, M., Farrow, K., and Bonin, V. (2018). Locomotion modulates specific functional cell types in the mouse visual thalamus. *Nat. Commun.* *9*, 4882.
21. Savier, E.L., Chen, H., and Cang, J. (2019). Effects of Locomotion on Visual Responses in the Mouse Superior Colliculus. *J. Neurosci.* *39*, 9360–9368.
22. Chen, C., and Regehr, W.G. (2003). Presynaptic modulation of the retinogeniculate synapse. *J. Neurosci.* *23*, 3130–3135.
23. Seeburg, D.P., Liu, X., and Chen, C. (2004). Frequency-dependent modulation of retinogeniculate transmission by serotonin. *J. Neurosci.* *24*, 10950–10962.
24. Yang, Y.-C., Hu, C.-C., Huang, C.-S., and Chou, P.-Y. (2014). Thalamic synaptic transmission of sensory information modulated by synergistic interaction of adenosine and serotonin. *J. Neurochem.* *128*, 852–863.
25. Lam, Y.-W., and Sherman, S.M. (2013). Activation of both Group I and Group II metabotropic glutamatergic receptors suppress retinogeniculate transmission. *Neuroscience* *242*, 78–84.
26. Liang, L., Fratzl, A., Goldey, G., Ramesh, R.N., Sugden, A.U., Morgan, J.L., Chen, C., and Andermann, M.L. (2018). A Fine-Scale Functional Logic to Convergence from Retina to Thalamus. *Cell* *173*, 1343–1355.
27. Gilzenrat, M.S., Nieuwenhuis, S., Jepma, M., and Cohen, J.D. (2010). Pupil diameter tracks changes in control state predicted by the adaptive gain theory of locus coeruleus function. *Cogn. Affect. Behav. Neurosci.* *10*, 252–269.
28. Idrees, S., Baumann, M.P., Franke, F., Münch, T.A., and Hafed, Z.M. (2020). Perceptual saccadic suppression starts in the retina. *Nat. Commun.* *11*, 1977.
29. Oommen, B.S., and Stahl, J.S. (2008). Eye orientation during static tilts and its relationship to spontaneous head pitch in the laboratory mouse. *Brain Res.* *1193*, 57–66.
30. Keller, G.B., Bonhoeffer, T., and Hübener, M. (2012). Sensorimotor mismatch signals in primary visual cortex of the behaving mouse. *Neuron* *74*, 809–815.
31. Saleem, A.B., Ayaz, A., Jeffery, K.J., Harris, K.D., and Carandini, M. (2013). Integration of visual motion and locomotion in mouse visual cortex. *Nat. Neurosci.* *16*, 1864–1869.
32. Sherman, S.M. (2001). Tonic and burst firing: dual modes of thalamocortical relay. *Trends Neurosci.* *24*, 122–126.
33. Schröder, S., Steinmetz, N.A., Krumin, M., Pachitariu, M., Rizzi, M., Lagnado, L., Harris, K.D., and Carandini, M. (2020). Arousal Modulates Retinal Output. *Neuron*, S0896-6273(20)30318-4.
34. Hauser, J.L., Edson, E.B., Hooks, B.M., and Chen, C. (2013). Metabotropic glutamate receptors and glutamate transporters shape transmission at the developing retinogeniculate synapse. *J. Neurophysiol.* *109*, 113–123.
35. McCormick, D.A., and Bal, T. (1994). Sensory gating mechanisms of the thalamus. *Curr. Opin. Neurobiol.* *4*, 550–556.
36. Pape, H.-C., and McCormick, D.A. (1989). Noradrenaline and serotonin selectively modulate thalamic burst firing by enhancing a hyperpolarization-activated cation current. *Nature* *340*, 715–718.
37. Varela, C., and Sherman, S.M. (2009). Differences in response to serotonergic activation between first and higher order thalamic nuclei. *Cereb. Cortex* *19*, 1776–1786.
38. Greferath, U., Kambourakis, M., Barth, C., Fletcher, E.L., and Murphy, M. (2009). Characterization of histamine projections and their potential cellular targets in the mouse retina. *Neuroscience* *158*, 932–944.
39. Farrow, K., Teixeira, M., Szikra, T., Viney, T.J., Balint, K., Yonehara, K., and Roska, B. (2013). Ambient illumination toggles a neuronal circuit switch in the retina and visual perception at cone threshold. *Neuron* *78*, 325–338.
40. Grimes, W.N., Schwartz, G.W., and Rieke, F. (2014). The synaptic and circuit mechanisms underlying a change in spatial encoding in the retina. *Neuron* *82*, 460–473.
41. Tikidji-Hamburyan, A., Reinhard, K., Seitter, H., Hovhannisyan, A., Procyk, C.A., Allen, A.E., Schenk, M., Lucas, R.J., and Münch, T.A. (2015). Retinal output changes qualitatively with every change in ambient illuminance. *Nat. Neurosci.* *18*, 66–74.
42. Pan, F. (2019). Defocused Image Changes Signaling of Ganglion Cells in the Mouse Retina. *Cells* *8*, 640.
43. Yüzgeç, Ö., Prsa, M., Zimmermann, R., and Huber, D. (2018). Pupil Size Coupling to Cortical States Protects the Stability of Deep Sleep via Parasympathetic Modulation. *Curr. Biol.* *28*, 392–400.
44. Fanselow, E.E., and Nicolelis, M.A.L. (1999). Behavioral modulation of tactile responses in the rat somatosensory system. *J. Neurosci.* *19*, 7603–7616.
45. Yoshida, M., Sasa, M., and Takaori, S. (1984). Serotonin-mediated inhibition from dorsal raphe nucleus of neurons in dorsal lateral geniculate and thalamic reticular nuclei. *Brain Res.* *290*, 95–105.

46. Marks, G.A., Speciale, S.G., Cobbey, K., and Roffwarg, H.P. (1987). Serotonergic inhibition of the dorsal lateral geniculate nucleus. *Brain Res.* *418*, 76–84.
47. Brainard, D.H. (1997). The Psychophysics Toolbox. *Spat. Vis.* *10*, 433–436.
48. Chen, T.-W., Wardill, T.J., Sun, Y., Pulver, S.R., Renninger, S.L., Baohan, A., Schreiter, E.R., Kerr, R.A., Orger, M.B., Jayaraman, V., et al. (2013). Ultrasensitive fluorescent proteins for imaging neuronal activity. *Nature* *499*, 295–300.
49. Lyubarsky, A.L., Daniele, L.L., and Pugh, E.N., Jr. (2004). From candelas to photoisomerizations in the mouse eye by rhodopsin bleaching in situ and the light-rearing dependence of the major components of the mouse ERG. *Vision Res.* *44*, 3235–3251.
50. Kerlin, A.M., Andermann, M.L., Berezovskii, V.K., and Reid, R.C. (2010). Broadly tuned response properties of diverse inhibitory neuron subtypes in mouse visual cortex. *Neuron* *67*, 858–871.
51. Storaice, D.A., Braubach, O.R., Jin, L., Cohen, L.B., and Sung, U. (2015). Monitoring brain activity with protein voltage and calcium sensors. *Sci. Rep.* *5*, 10212.
52. Sun, W., Tan, Z., Mensh, B.D., and Ji, N. (2016). Thalamus provides layer 4 of primary visual cortex with orientation- and direction-tuned inputs. *Nat. Neurosci.* *19*, 308–315.
53. Piscopo, D.M., El-Danaf, R.N., Huberman, A.D., and Niell, C.M. (2013). Diverse visual features encoded in mouse lateral geniculate nucleus. *J. Neurosci.* *33*, 4642–4656.
54. Mastronarde, D.N. (1985). Two types of cat retinal ganglion cells that are suppressed by contrast. *Vision Res.* *25*, 1195–1196.
55. Tien, N.-W., Pearson, J.T., Heller, C.R., Demas, J., and Kerschensteiner, D. (2015). Genetically Identified Suppressed-by-Contrast Retinal Ganglion Cells Reliably Signal Self-Generated Visual Stimuli. *J. Neurosci.* *35*, 10815–10820.
56. Li, D., Winfield, D., and Parkhurst, D.J. (2005). Starburst: A hybrid algorithm for video-based eye tracking combining feature-based and model-based approaches. 2005 IEEE Computer Society Conference on Computer Vision and Pattern Recognition Cvpr'05 - Workshops, p. 79.
57. Bhattacharyya, A. (1943). On a measure of divergence between two statistical populations defined by their probability distributions. *Bull. Calcutta Math. Soc.* *35*, 99–109.

STAR★METHODS

KEY RESOURCES TABLE

REAGENT or RESOURCE	SOURCE	IDENTIFIER
Virus Strains		
AAV2/2.CAG.GCaMP6f.WPRE.SV40	Boston Children's Hospital Viral Core	N/A
Experimental Models: Organisms/Strains		
Mouse: C57BL/6J	Jackson	RRID: IMSR_JAX:000664
Software and Algorithms		
Prism 8	GraphPad	https://www.graphpad.com/ ; RRID: SCR_002798
MATLAB R2017b	Mathworks	https://www.mathworks.com/products/matlab.html ; RRID: SCR_001622
ImageJ 1.49t	NIH	https://imagej.nih.gov/ij/ ; RRID: SCR_003070
Psychtoolbox-3	[47]	http://psychtoolbox.org/
Scanbox	Neurolabware	https://scanbox.org/
Other		
20x, 1.0 NA objective	Carl Zeiss Microscopy	Cat#421459-9770-000
4x, 0.28 NA objective	Olympus	XLFLUOR
Two-photon microscope	Neurolabware	http://neurolabware.com/
Ti:Sapphire laser	Spectra-Physics	Mai Tai HP DeepSee
InSight X3 laser	Spectra-Physics	InSight X3
sCMOS camera	PCO	Pco.edge 3.1

RESOURCE AVAILABILITY

Lead Contact

Further information and requests for resources and reagents should be directed to and will be fulfilled by the Lead Contact, Mark L. Andermann (manderma@bidmc.harvard.edu).

Materials Availability

This study did not generate new unique reagents.

Data and Code Availability

The widefield and two-photon fluorescence imaging datasets and analysis code supporting the current study have not been deposited in a public repository due to the large data size, but are available from the Lead Contact on request.

EXPERIMENTAL MODEL AND SUBJECT DETAILS

All animal care and experimental procedures were approved by the Beth Israel Deaconess Medical Center Institutional Animal Care and Use Committee. Animals were housed with standard mouse chow and water provided *ad libitum*. Male C57BL/6 adult mice (2-6 months old) were used in this study.

METHOD DETAILS

Viral injection

To label retinal ganglion cell axons, 1.2 μ l of AAV2/2.CAG.GCaMP6f.WPRE.SV40 [48]; Boston Children's Hospital Viral Core) was gently injected intravitreally into the right eye after the mouse was anesthetized using isoflurane in 100% O₂ (induction, 3%–5%; maintenance, 1%–2%). Care was taken to minimize bleeding and to prevent cataract formation during the injection procedure.

Headpost and cranial window implantation

A headpost and cranial window were implanted 2-3 weeks after viral injection. Mice were given 0.03 mL of dexamethasone sodium phosphate (4 mg/mL, i.m.) roughly 3 h prior to surgery in order to reduce brain edema. Mice were anesthetized using isoflurane in 100% O₂ (induction, 3%–5%; maintenance, 1%–2%) and placed on a heating pad (CWE) in a stereotaxic apparatus (KOPF).

Ophthalmic ointment (Vetropolycin) was applied to the eyes. Using a procedure similar to that described previously [26], a two-pronged headpost was affixed to the skull, centered roughly 2.7 mm lateral and 1.9 mm posterior to Bregma over the left hemisphere, tangential to the curved skull surface. The head was then tilted to secure the headpost in custom clamps (Thorlabs, Standa) that aligned the headpost precisely parallel to the platform of the stereotaxic apparatus. A 3-mm diameter craniotomy was performed at the center of the headpost. The underlying cortical and hippocampal tissue was carefully aspirated until reaching the surface of the thalamus. The thalamic surface and optic tract were kept intact. A 3-mm diameter coverslip (glued to the bottom of a 3 mm x 3.4 mm (diameter x height) stainless steel cylindrical cannula (MicroGroup) prior to surgery using UV-cured Norland Optical Adhesive 71) was lowered into the craniotomy, approximately 2.75 mm below the skull, where it pressed slightly on the surface of the thalamus. The cannula was affixed to the skull with Vetbond (3M) followed by C&B Metabond (Parkell), to form a permanent seal. To create a low-profile adaptor to accommodate the water-immersion objective and light shielding, a neodymium ring magnet (Indigo® Instruments, outer diameter, inner diameter, height: 7.5 mm, 5 mm, 1 mm) was positioned around the cannula and glued to the skull. During two-photon imaging sessions, this ring magnet held the light shielding in place by contact with a 8 mm x 0.3 mm (diameter x height) spring steel round shim (McMaster) attached to the blackout fabric (Thorlabs). Meloxicam (0.5 mg/kg, s.c.) was administered and the mouse was allowed to recover.

Epifluorescence and two-photon calcium imaging

To measure bulk calcium signals in response to visual stimulation in head-fixed mice across arousal states, we performed epifluorescence calcium imaging (NeuroLabware). A blue LED light source (470 nm center, 40 nm band, Chroma) was used for excitation, and the green fluorescence was passed through a 500 nm long-pass emission filter and collected using a sCMOS camera (PCO). Light shielding around the objective was used to block light emitted by the LCD screen. We focused on the surface of the thalamus. Epifluorescence images (512 × 384 pixels) were acquired at 15.5 Hz, using a 4x, 0.28 NA objective (Olympus).

Two-photon calcium imaging was performed using a resonant-scanning two-photon microscope (NeuroLabware). All images were acquired using a 20x, 1.0 NA, 5.6 mm WD objective (Zeiss) at 4.7x (~160 × 210 μm²) or 2.8x (~95 × 125 μm²) digital zoom. Light shielding around the objective was used to block light emitted from the LCD screen. We concentrated on imaging fields of view (FOV) at depths of 80–150 μm below the surface of the optic tract (roughly corresponding to the upper 20–90 μm of the dLGN shell; high-quality images could be obtained throughout the upper ~140–150 μm of the dLGN, data not shown), using a MaiTai HP DeepSee Ti:Sapphire laser (80 MHz; Spectra-Physics) or an Insight X3 laser (80 MHz; Spectra-Physics) at 960 nm. The arousal modulation results were not sensitive to imaging depth within this range (not shown). Laser power measured at the front aperture of the objective was 30–65 mW – likely a substantial overestimate of actual power reaching the sample via the cannula. Images were collected at 15.5 frames/s, 686 × 512 pixels/frame, using Scanbox (NeuroLabware). Each imaging run lasted approximately 30 min, and 4–5 runs were performed during each imaging session. Occasionally, the imaging depth was adjusted slightly in between runs to account for slow drifts in the z-plane. For a given mouse, each FOV imaged in a given session was at least 20 μm above or below any FOV imaged in another session. Epifluorescence and two-photon imaging experiments were typically performed between one week and one month after headpost and cranial window implantation.

Pupil videography and image analysis

During epifluorescence imaging, the eye contralateral to visual stimulation was illuminated by an infrared LED. During two-photon imaging, the pupil ipsilateral to the LCD screen was illuminated by the spread of two-photon excitation infrared light emanating from within the brain. Images of a pre-selected region of interest around the eye were recorded using a CCD camera (Dalsa) at 15.5 Hz, synchronized with fluorescence image acquisition (Scanbox, NeuroLabware).

Locomotion during two-photon imaging

Locomotion was recorded using a customized rotary encoder at a resolution of 0.5 cm/step. Total distance traveled was registered at 15.5 Hz, synchronized with two-photon image acquisition (Scanbox, NeuroLabware). The running speed was calculated as the displacement between two adjacent data points dividing by the time between data points (~.065 s), and smoothed by a median filter (width: 5 samples, or ~.32 s).

Visual Stimulation

Visual stimuli were generated using Psychtoolbox [47], and displayed on a luminance-calibrated LCD monitor (Dell, 17,"1280 × 1024 pixels, 60 Hz refresh rate) placed 22 cm from the mouse's right eye and spanning 80° × 70° of visual space (azimuth: –40° to 40°, with 0° indicating the line perpendicular to the eye, which is ~45° lateral to the axis in front of the head, see Figure 4D; elevation: –13° –57° relative to this same line). We estimated the luminance with the LCD on and at mean luminance to be 4.8 lux at the mouse's ipsilateral eye. Based on calculations from [49], we could obtain a very rough estimate that during median pupil areas in the low arousal and high arousal state, this luminance would result in ~40 and ~200 photoisomerizations/rod/s – in other words, the effective illumination of the retina using our stimulus conditions spans the upper scotopic to lower mesopic range of vision.

To measure arousal modulation during epifluorescence imaging, we presented full-screen sine-wave drifting gratings (80% contrast) at 0° (nasal to temporal direction) and at spatial frequencies of 0.02, 0.08 and 0.32 cycles per degree (cpd) and a temporal frequency of 2 Hz. Gratings of different spatial frequencies were delivered in a random order, with blank trials (full-screen mean luminance – gray screen) interleaved in between. All stimuli were displayed for a 2 s duration. The inter-stimulus interval (mean luminance

gray) lasted 2 s. One session consisted of 432 repeats of gratings at each spatial frequency and 108 blank trials. Each animal was recorded on two different sessions on two consecutive days.

To measure arousal modulation during two-photon imaging, we presented full-screen 2 Hz sine-wave drifting gratings (80% contrast) at eight directions of motion spaced 45° apart for each of the three spatial frequencies of 0.02, 0.08 and 0.32 cycles per degree. The visual stimulation paradigm also included periods of full-screen mean luminance (gray, blank trials) or periods of full-screen bright or dark screen ('On' or 'Off' trials, respectively, 80% contrast). All stimuli were displayed for a 2 s duration. The inter-stimulus interval (mean luminance gray) lasted 2 s. A single repeat involved presentation, in random order, of the set of all of the above stimuli (one presentation of each direction and spatial frequency, three presentations of 'On' and 'Off' stimuli, and three or six presentations of 'blank' stimuli). A single run usually consisted of 10-14 repeats, each with a different randomized stimulus order. We recorded 3-5 runs for each FOV in a given imaging session.

To measure retinotopy with high spatial resolution during two-photon imaging, we used a binarized version of a bandpass-filtered noise stimulus with a spatial frequency corner of 0.05 cycles per degree, a cutoff of 0.32 cycles per degree and a temporal frequency cutoff of 4 Hz [2]. The noise stimulus was presented within 5° × 40° bars, presented vertically at one of 8 azimuth locations and horizontally at one of 8 elevations. Stimuli were presented for 2 s each, with a 2 s inter-stimulus interval (mean luminance, gray). Visual stimulation also included a blank condition (mean luminance, gray). Stimulus order was randomized within a single repeat (consisting of a single presentation of each stimulus condition), and 30 repeats were presented during one run. We performed 1-2 runs of retinotopic mapping per imaging session.

Image processing

Image preprocessing

To correct for x-y motion along the imaged plane, a series of image registration and data cleaning steps were applied [26]. For epifluorescence images, movies collected on each imaging day were registered to a common average field-of-view using a local image normalization method (subtraction of local mean and division by local variance across pixels) and an image warping method (imregdemons.m, MATLAB, Mathworks; <https://www.mathworks.com/help/images/ref/imregdemons.html>). For two-photon images, additional denoising method was implemented to aid image registration. Specifically, principal component analysis (PCA) was performed to identify spatial principal components of the field of view and each image of the movie was reconstructed using only the first 400 (highest eigenvalues) out of ~30,000 principle components. The denoised images were then subjected to local normalization and image warping to derive the warping parameters, which were then applied to the original raw movie. For additional details, please see [26].

Identification of the responsive region in the dLGN from bulk calcium imaging

The dLGN region could be easily distinguished from superior colliculus or other thalamic regions, based on baseline green fluorescence from GCaMP6f-expressing retinal ganglion cell axons, and from the characteristic oval shape. However, given the limited dimensions of the LCD monitor used for displaying visual stimuli, and the obstructions in the upper visual field due to light shielding, not all the dLGN regions receiving RGC projection responded to visual stimulation. For quantifying calcium signals across arousal states, we only considered the portion of the dLGN that showed robust visually evoked responses during at least one of the stimulus conditions (spatial frequencies). We first generated four mean $\Delta F/F$ images, one for stimuli at each of the three spatial frequencies used, and one for blank trials. We then generated a single image that was the mean intensity projection of these four images. We compared multiple methods for defining the portion of the dLGN with active responses. Ultimately, we defined the responsive region as the set of 5000 pixels within the dLGN that showed the strongest evoked response in the mean intensity projection image. This ensured comparable shot noise in the average time courses estimated from each session. Control analyses in which we further dilated this region (not shown) indicated that the modulation index was generally stable regardless of the parameters used to define the active subregion of the dLGN.

Identification of bouton masks

To identify boutons and extract masks for further signal processing, we established an automated image segmentation algorithm. First, an image of the absolute value of the average $\Delta F/F$ was calculated for each trial type by averaging single condition evoked response maps across all N repetitions of that trial type [$\text{mean}((F_i - F_{i0})/F_{i0})$, $i = 1..N$, where F_i is the mean fluorescence during the stimulus presentation and F_{i0} is the average baseline fluorescence during the 1 s prior to each stimulus onset]. We used the absolute value of $\Delta F/F$ in order to include boutons that were strongly suppressed by visual stimuli, corresponding to negative values of $\Delta F/F$. A bouton identification procedure was then independently applied to each of these average $\Delta F/F$ images. First, local normalization was applied, with the local mean estimated by isotropic filtering of the image using a Gaussian kernel (with standard deviation, $\sigma = 3 \mu\text{m}$). The local variance was estimated using a larger Gaussian filter ($\sigma = 50 \mu\text{m}$).

Morphological filters were then applied to identify, in an unbiased manner, connected sets of pixels that together resembled the size and shape of a typical RGC bouton, as follows: first, small pixel gaps were filled by interpolation using a square-shaped structuring element of $1.3 \times 1.3 \mu\text{m}^2$. We then removed all small unconnected structures via an 'opening' operation using the same structuring element. To obtain candidate masks, we first binarized the above images by setting to '1' all pixels with values above 10% to 15% of the maximal pixel amplitude after filtering, and setting all other pixels to '0'. A Euclidian distance transform was then applied to these binary images (MATLAB function 'bwdist.m', <https://www.mathworks.com/help/images/ref/bwdist.html>). The built-in MATLAB watershed transform was used to finalize the segmentation (MATLAB function 'watershed.m', <https://www.mathworks.com/help/images/ref/watershed.html>). The results from the distance transform and the watershed transform from the individual

$\Delta F/F$ images were combined by summing the distance transform across conditions and normalizing this value by the bouton count obtained by the watershed transformation. A final watershed transformation was applied to this normalized distance image to increase the accuracy of the procedure and to reduce the risk of false positives in the bouton identification procedure. In addition, to remove residual calcium signals not originating from the bouton itself, we estimated neuropil masks as circular annuli of $3\ \mu\text{m}$ width, with the inner edge located $2\ \mu\text{m}$ beyond the edge of a corresponding bouton mask. Pixels from adjacent bouton masks were excluded from these neuropil masks.

Time course extraction and correction

To obtain raw fluorescence traces for dLGN region in epifluorescence imaging datasets, or for bouton masks and neuropil masks in two-photon imaging datasets, the fluorescence intensity value at each time point was defined as the average fluorescence across the pixels belonging to the region or to the mask.

To account for photobleaching during two-photon imaging sessions, a bleaching correction method was established. Raw bouton and neuropil traces were first smoothed using a sliding filter (30th percentile of a 5-min sliding window). Then, the filtered traces were fitted using a decaying exponential, where the amplitude and the offset were independently estimated for each bouton and each neuropil ring, while the time constant was fixed to an experimentally defined constant value of 75 min, which was in agreement with time constants other groups have determined for the photobleaching of GCaMP6f using two-photon imaging at similar excitation wavelengths and laser power (Harris lab/Photophysics, <https://www.janelia.org/lab/harris-lab-apig/research/photophysics/two-photon-fluorescent-probes>). To correct for photobleaching in each trace, the fitted offset value was first subtracted from the raw trace, and then the resulting trace was multiplied by the inverse of the exponential of the fixed decay time constant before adding back the offset value.

To account for neuropil signals which may contaminate signals in the bouton trace, neuropil correction was applied by subtracting a scaled version of the corresponding neuropil trace ($0.6 \times$ neuropil trace) from each bouton trace before adding back the mean neuropil fluorescence (temporally-averaged across the neuropil trace) [50].

To account for autofluorescence from brain tissue in the epifluorescence image, we estimated the average fluorescence value from a region anterior to the dLGN which received no RGC input, which served as approximation of the level of background autofluorescence. We subtracted this estimate on a frame-by-frame basis from the fluorescence trace of the identified dLGN region.

We also corrected baseline fluorescence, F_0 , to remove the decay in fluorescence from activity evoked during the previous visual stimulus presentation. Due to slow decay dynamics *in vivo* (as a result of calcium buffering and GCaMP6f buffering) after stimulus-evoked calcium activity, the bouton fluorescence sometimes did not fully return to baseline during the 1 s after the offset of the previous stimulus presentation, and persisted in the 1 s used to calculate F_0 for the following stimulus period. Therefore, a baseline correction was introduced that modeled this exponential decay of previously evoked GCaMP6f calcium activity, using an experimentally determined fixed time constant of 1 s (in agreement with previously determined GCaMP6f dynamics *in vivo* [51]): $F_{\text{prev-fit}}(t) = a \cdot \exp(-t/\tau) + c$, where τ is the time constant and c is the new corrected F_0 .

To assess the fractional change in fluorescence, $\Delta F/F(t)$, during each visual stimulus presentation, the fitted, exponentially decaying contribution from the previous trial was first subtracted from $F(t)$ during the 1 s interval prior to and the 2 s interval during visual stimulus presentation. Then, the corrected baseline was used as the new baseline F_0 to compute $\Delta F/F(t)$. Single response values during a given trial were obtained by averaging the $\Delta F/F(t)$ response during the 2 s stimulus window.

Estimation of visual tuning preferences in RGC boutons

Estimation of boutons with significant visual responses

We define single condition bouton responses in two-photon imaging datasets as the average from all the trials of a given stimulus condition. Visually evoked responses were corrected by subtracting the average response across blank trials. There were approximately 30 repeats for each of the retinotopic conditions, 60 trials for each combination of direction and spatial frequency (SF), 180 trials of luminance increments and decrements ('On' and 'Off') and 360 blank trials. Different boutons had differing response dynamics, and we attempted to minimize bias in which boutons were deemed significantly visually responsive. Thus, we assessed, for each bouton and each stimulus condition, if the evoked response was significantly different from noise, by requiring the amplitude of $\Delta F/F(t)$ during the response window to exceed 2.5 standard deviations above or below the mean baseline activity (computed using the 1 s window prior to stimulus onset) for at least 10 out of the 31 time points (15.5 Hz frame rate \times 2 s stimulus presentation). For assessment of significant On and Off responses, we only required the $\Delta F/F(t)$ amplitude to exceed this threshold for at least 5 of the 31 time points, as a substantial proportion of boutons exhibited transient On and/or Off responses. These criteria were confirmed to be highly conservative, thereby including only highly robustly visually responsive boutons.

To assess if a given bouton exhibited a *significantly positive response* at a particular spatial frequency, we required that at least 3 out of the 8 directions at this spatial frequency evoked significantly positive responses according to the criteria described above. A similar approach was used to determine if a bouton exhibited a significantly negative response to a particular spatial frequency. Note that all boutons contributing to the main results underwent additional quality controls (see below), further protecting against inclusion of any noisy boutons in our analyses.

Direction tuning curve fitting

For each bouton showing a significantly positive response at a given spatial frequency, a direction tuning curve was computed across directions for stimuli presented at that spatial frequency. The direction tuning curves were initially sampled in steps of 45° . In order to

obtain a more precise estimate of the preferred axis and direction, a fitting approach was used to estimate the preferred direction. Tuning curves were fitted with a two-peaked Gaussian with offset [52]:

$$R(\theta) = R_1 e^{-\frac{(\theta - \theta_{pref})^2}{2\sigma^2}} + R_2 e^{-\frac{(\theta - \theta_{pref} - 180^\circ)^2}{2\sigma^2}} + R_{off}$$

$R(\theta)$ was the $\Delta F/F$ response for stimulus direction θ . This model assumed that the peaks of the two Gaussians were 180° apart. θ_{pref} was defined as the preferred direction evoking the strongest $\Delta F/F$ response, $R_1 \cdot R_2$ was the amplitude of the second peak located at $\theta_{pref} + 180^\circ$. It was also assumed that both Gaussians shared a common standard deviation, σ . The fifth fitted parameter was a constant amplitude offset, R_{off} .

Several steps were taken to improve the reliability of the fitting of direction tuning curves and to optimize the accuracy of estimation of preferred direction of motion. To increase the number of input points for the fitting procedure from 8 to 25, a heuristic method of interpolation and extrapolation was implemented. First, a ninth point was added at 360° , which was identical to the one at 0° . Then, the number of input points was doubled from 9 to 17 by linear interpolation of the 9-point direction tuning curve. For the interpolated data point between the two most strongly driven initial directions (out of 9), we further adjusted the interpolated amplitude so that its value became a close approximation of that predicted point from a Gaussian curve fit through the rest of the points, thus reducing the error introduced by linear interpolation given the expected continuity of the curves. To this end, we applied the empirical formula described below. Note that our results were largely unchanged if this additional adjustment to the linear interpolation was omitted (mean difference in preferred direction: 2° , median difference: 1.2°). However, this additional peak adjustment resulted in significantly smaller residual values between the fitted curve and the initial 8-direction tuning curve.

The interpolated amplitude between the two most strongly driven initial directions was calculated as follows. R_{S1} was defined as the strongest response out of all 8 directions and R_{S2} as the stronger of the two responses for directions $\pm 45^\circ$ adjacent to R_{S1} . R_{S3} was defined as the weaker of the two responses adjacent to R_{S1} . R_{S4} was defined as the response adjacent to R_{S2} , at 90° from R_{S1} . The interpolated $\Delta F/F$ response R_{S12} between R_{S1} and R_{S2} was defined as: $R_{S12} = (R_{S1} + R_{S2})/2 + (1/6)(1 - (R_{S1} - R_{S2})/(R_{S1} - R_{S3}))((R_{S1} - R_{S3}) + (R_{S2} - R_{S4}))$. This method compared the slope between R_{S1} and R_{S2} with the slope between R_{S1} and R_{S3} . If the peak was flat, a maximum amount of $(1/6)((R_{S1} - R_{S3}) + (R_{S2} - R_{S4}))$ was added, corresponding roughly to the expected value of a Gaussian peak. If the absolute values of the slopes between R_{S1} and R_{S2} and between R_{S1} and R_{S3} were identical (and therefore R_{S1} was the real peak of the Gaussian), this corresponds to $(1 - (R_{S1} - R_{S2})/(R_{S1} - R_{S3})) = 0$ in the above equation, therefore resulting in no additional value added to the interpolation method. A similar method was used to interpolate negative peaks.

To further improve the stability of the fitting procedure and to better approximate the direction tuning curve, we added two shadow-copies of the two-peaked Gaussian function, circularly shifted by $+360^\circ$ and -360° :

$$R_{fit}(\theta) = R_1 \left(e^{-\frac{(\theta - \theta_{pref})^2}{2\sigma^2}} + e^{-\frac{(\theta - \theta_{pref} - 360^\circ)^2}{2\sigma^2}} + e^{-\frac{(\theta - \theta_{pref} + 360^\circ)^2}{2\sigma^2}} \right) + R_2 \left(e^{-\frac{(\theta - \theta_{pref} - 180^\circ)^2}{2\sigma^2}} + e^{-\frac{(\theta - \theta_{pref} - 540^\circ)^2}{2\sigma^2}} + e^{-\frac{(\theta - \theta_{pref} + 180^\circ)^2}{2\sigma^2}} \right) + R_{off}$$

This addition of the shadow-copies increased the range to $[-90^\circ, 450^\circ]$, and thus extended the fitted tuning curve by 4 additional directions (at 22.5° spacing) on either end. While the adjusted linear interpolation and the addition of the shadow copies improved the fitting procedure, similar results were obtained using the basic 17-point linearly interpolated tuning curve (data not shown)

A bootstrapping method involving random sampling of trials from each condition was then implemented to fit the tuning curves. Specifically, for each of 100 iterations, the tuning curve was initially computed by randomly sampling with replacement, and by averaging responses from 60 trials sampled from each of the 8 directions. These 8-point tuning curves were then interpolated, extended and finally fitted using the method described above. The final parameters used were the mean of the fitted parameters across the 100 sampling iterations.

To determine if the fitting procedure yielded a high-quality fit, a combination of criteria was used. Each iteration of the fitting procedure yielded a coefficient of determination, r^2 , defined as the explained variance using least-squares regression to fit the data. As a second control step, a combined coefficient of determination, r_{comb}^2 , was computed by comparing the original direction tuning curve with the fitted curve derived using the average of each fitting parameter (across 100 iterations). To assess both the quality and the reliability of the fitting procedure, we introduced a heuristic goodness of fit, G_{fit} :

$$G_{fit} = \sqrt{r^2} \left(1 - IQR(\sqrt{r^2}) \right) \sqrt{r_{comb}^2}$$

where IQR was defined as the interquartile range – the difference between the 75th-percentile and the 25th-percentile (of $\sqrt{r^2}$ values across iterations). A bouton was considered to have a well-fit direction tuning curve at a given spatial frequency if the goodness of fit, G_{fit} , was greater than 0.66. The threshold was chosen based on examination of a large proportion of example boutons, and values in the range of 0.5 to 0.9 yielded similar results. The complete direction curve fitting procedure was separately run for each of the three spatial frequencies employed, and therefore each bouton was attributed up to three sets of fitting parameters.

Axis and direction selectivity

For each bouton, we calculated its axis and/or direction selectivity at a given spatial frequency if we observed a significantly positive evoked response at that spatial frequency. For axis selectivity, we calculated a ‘vector sum’ axis selectivity index (ASI [53]; i.e., selectivity for a motion along a given axis) on each interpolated direction tuning curve. This index was calculated by projecting the $\Delta F/F$

response for each of the 16 directions in the range between 0° and 360° onto a circle with $2i$ progression and estimating the magnitude of the normalized vector sum, which ranged from 0 to 1 (maximum selectivity): $ASI = \left(\left| \sum_{n=1}^{16} R(\theta_n) e^{\frac{2i \cdot 2\pi \theta_n}{360^\circ}} \right| \right) / \left(\sum_{n=1}^{16} |R(\theta_n)| \right)$.

Opposite directions contributed in an additive fashion, while orthogonal directions canceled each other out. The ASI computation was iterated 100 times by bootstrapping and averaged for each spatial frequency.

In a similar manner, we computed a ‘vector sum’ direction selectivity index (DSI [53]), by projecting the 16 directions onto a circle with $1i$ progression: $DSI = \left(\left| \sum_{n=1}^{16} R(\theta_n) e^{\frac{1i \cdot 2\pi \theta_n}{360^\circ}} \right| \right) / \left(\sum_{n=1}^{16} |R(\theta_n)| \right)$. As with ASI, the DSI estimate was repeated with the bootstrapping method, and the average was used as the DSI for that spatial frequency.

Preferred direction of motion and preferred axis of motion

For direction-selective boutons or axis-selective boutons, the preferred direction of motion or preferred axis of motion was defined as the direction or axis of the mean vector across the preferred motion direction or motion axis for each spatial frequency, which was the direction or axis with peak response amplitude estimated from the fitted tuning curve at the given spatial frequency. Estimates of preferred direction or axis of motion ranged from 0° and 360°, or 0° and 180°, respectively.

To compensate for the pitch angle of the mouse head during imaging acquisition (Pitch of 31.6° above the angle estimated for a typical ambulatory position [29]; Roll: 16.7°; measured using stereotaxic coordinates during headpost implant, N = 3 mice), we rotated the preferred direction or axis of motion counterclockwise by 31.6°.

OnOff preference index

An OnOff preference index was calculated using the averaged response traces to luminance increments (On stimulus) and to luminance decrements (Off stimulus). A positive response to On only, to Off only, or a positive response of equal magnitude to On and Off corresponded to index values of 1, −1 or 0, respectively. Boutons lacking both a significant On response and a significant Off response (see Subsection, ‘Estimation of boutons with significant visual responses’) were not considered.

In order to take into account the dynamics of the evoked On and Off responses, a weighted OnOff preference index was introduced as follows:

$$OnOff_{pref} = \frac{(On_t - Off_t) \cdot (|On|_t + |Off|_t)}{\| |On|_t + |Off|_t \|^2}$$

On_t and Off_t were defined as the On and Off response time courses during the 2 s response window. In this equation, the term $(On_t - Off_t)$ determines the sign of the index at each time point. The dot product of this term with $(|On|_t + |Off|_t)$ was used to assign a relative weight to each time point according to its summed response magnitude. Then the numerator was normalized to obtain a single preference index between −1 and 1.

A subset of SbC boutons exhibited a positive rebound after transient suppression [54, 55]. The positive values in On and Off response traces from those boutons were set to zero prior to estimating OnOff preference. Moreover, we added a minus sign to the above formula, so that SbC boutons that were significantly suppressed by an On stimulus were defined as On-responsive SbC, while SbC boutons that were significantly suppressed by an Off stimulus were defined as Off-responsive. While this is opposite to our previous definition for SbC cells [26], it increased clarity in this study by enabling consistent interpretation of arousal modulation across bouton classes.

Bouton type classification

A bouton was classified as direction selective if, for at least one of the three spatial frequencies used, (i) it had a significant positive response, (ii) the tuning curve was successfully fit (as estimated by goodness of fit criteria), (iii) the direction selectivity index (DSI) exceeded 0.2 (a value equivalent to 0.33 if direction selectivity was calculated as $DSI = (R_{pref} - R_{opp}) / (R_{pref} + R_{opp})$, where R_{pref} was the response at the preferred direction and R_{opp} was the response at the opposite direction). Additionally, for all spatial frequencies which showed a significant positive response, we also required the DSI at each of these spatial frequencies to exceed 0.15 (to ensure that group assignment was not sensitive to the vagaries of which spatial frequencies were used). Finally, we verified that boutons in this group did not show any significantly negative responses for any spatial frequency.

A bouton was defined as axis selective (i.e., most strongly responsive to motion along two opposite directions constituting a single axis of motion) if (i) it had at least one significantly positive response for at least one of the three spatial frequencies, (ii) the fitting procedure was reliable, and (iii) the axis selectivity index (ASI) exceeded 0.15 (a value equivalent to 0.33 if axis selectivity was calculated as $ASI = (R_{pref} - R_{orth}) / (R_{pref} + R_{orth})$, where R_{pref} was the response at the preferred direction and R_{orth} was the mean response at the two directions orthogonal to the preferred one). We distinguish the term axis selectivity from orientation selectivity, as the latter is often used even for responses to stationary (i.e., non-drifting) oriented gratings – a stimulus not examined in this study. It is possible that certain axis selective boutons may not be strongly driven by stationary gratings. For all spatial frequencies for which we observed a significant positive response, we further required that the DSI was less than 0.2 and that the ASI was greater than 0.1. If these conditions were not met or if the bouton showed any significant negative response at any spatial frequency, the bouton was removed from this group.

A bouton was defined as ‘broadly tuned’ if (i) it exhibited a significant positive response for at least one of the three spatial frequencies and (ii) the ASI and DSI were below 0.15 and 0.2, respectively, for all significant spatial frequencies. We also removed boutons that exhibited any significant negative responses at any spatial frequency.

Boutons having significant negative responses for at least one spatial frequency and no significant positive response at any spatial frequency were defined as ‘suppressed’. ‘Suppressed-by-contrast’ (SbC) boutons were further defined as those boutons generally suppressed by all types of visual stimuli, including horizontal and vertical bars containing spatiotemporal noise (used for retinotopic mapping). Moreover, a SbC bouton needed to be significantly suppressed by at least 2 out of the 8 retinotopic conditions in at least one of the two stimulation axes. If no retinotopic mapping stimulus evoked a significant response, or if the response to one or both retinotopic stimulation axes was significantly positive, the bouton was classified as ‘suppressed’, but not as part of the subcategory of ‘SbC’ boutons. Only the SbC subcategory of suppressed boutons was considered in this study.

Boutons which showed a significant visually-evoked response but were not classified into any of the above conservatively-defined categories, were ‘unclassified’ boutons and were not included in subsequent analyses.

Finally, a small proportion of candidate bouton masks were not significantly driven by any of the presented visual stimuli. These were classified as ‘unresponsive’ and not considered further.

Arousal modulation

The arousal level of the mouse was assessed by estimating pupil area [6–8, 12, 27]. Pupil area was automatically identified from the acquired videos using customized scripts in MATLAB (MathWorks). To fit pupil regions recorded during two-photon imaging with ellipses and extract pupil parameters including centroid positions, widths and heights, the Starburst algorithm was used [56]. For extracting the pupil parameters when recorded during epifluorescence imaging, morphological filters and the grayconnected.m function (MATLAB, MathWorks, <https://www.mathworks.com/help/images/ref/grayconnected.html>) were first used to identify the region of image that belonged to the pupil, due to the difference in pupil illumination methods between epi and two-photon imaging. The regionprops.m function (MATLAB, Mathworks, <https://www.mathworks.com/help/images/ref/regionprops.html>) was then used to fit an ellipse to the pupil region and to measure parameters of the ellipse, including the centroid position, the width and the height. For both methods, pupil area was calculated as the area of the fitted ellipse, normalized to the maximal pupil area during each session, and temporally smoothed by a median filter (width: 5 adjacent frames).

The distribution of pupil areas in each session was then assessed, and the area values at 25% and 75% were selected as thresholds for low arousal and high arousal states. For each trial, the average pupil area estimate from 1 s before to 2 s after onset of visual stimulation was computed and used as the pupil area for that trial. If the average pupil area for a given trial was below the 25% threshold, the mouse was considered to be in a low arousal state during that trial. If the average pupil area was above the 75% threshold, the mouse was considered to be in a high arousal state.

To quantify the degree of arousal modulation of responses of drifting gratings, we defined a modulation index, $MI = [R_{\text{HighArousal}} - R_{\text{LowArousal}}] / R_{\text{AllTrials}}$, where $R_{\text{HighArousal}}$, $R_{\text{LowArousal}}$, $R_{\text{AllTrials}}$ represent the average response across all high arousal trials, the average response across all low arousal trials, and the average response across all trials, respectively. Note that, because responses tended to vary linearly and were anticorrelated with pupil area, the value of $R_{\text{AllTrials}}$ was roughly similar to the value of $([R_{\text{HighArousal}} + R_{\text{LowArousal}}]) / 2$, which is more commonly used as the denominator for such an index. Note that the index that we use is thus roughly similar to $2 * [R_{\text{HighArousal}} - R_{\text{LowArousal}}] / [R_{\text{HighArousal}} + R_{\text{LowArousal}}]$. For epifluorescence imaging, the response magnitudes (R-values) were computed to 0° drifting gratings. For individual boutons from two-photon imaging, we considered three directions: the direction that drove the maximal response, and the two adjacent directions (spaced $\pm 45^\circ$ apart). We first calculated the average response across trials for each of the three directions, and then averaged this value across the three directions. On average, 11.8 ± 1.0 trials (mean \pm SEM) were included as low arousal trials, and 15.7 ± 1.7 trials were included as high arousal trials, for each direction at the intermediate spatial frequency (22 FOV, 5 mice). No single direction had fewer than 2 trials at low or high arousal states, and no 3 used adjacent directions had fewer than 9 trials in total at low or high arousal states. To further remove noisy boutons for a given spatial frequency, we also required that DS, AS, BrT and SbC boutons satisfy the above defined criteria for direction-selective, axis-selective, broadly-tuned, or suppressed-by-contrast, respectively. Moreover, for DS, AS and BrT boutons, we required the mean responses across the peak direction and two adjacent directions to be positive at both low and high arousal; for SbC boutons, we required the mean responses to be negative at both low and high arousal. Due to these additional criteria, the total number of boutons used for calculating the modulation index was smaller than the number of boutons used for calculating correlation with pupil area.

For each bouton, we also assessed whether arousal modulation was significant ($p < 0.05$). An N-way ANOVA was used to compare the responses from the aforementioned three directions (direction of maximal response and adjacent directions), at low versus high arousal. To obtain the fraction of boutons that would have been deemed significantly suppressed or significantly enhanced in randomized data, we performed random shuffling analysis. For each bouton, we shuffled the mean single-trial responses across all trials under the same visual stimulus condition in the session while maintaining the same trial-by-trial sequence of arousal states as was present in the original data, and recalculated the p values. We measured the fraction of significant boutons from each shuffle, and repeated this procedure 1000 times. We then displayed the median value (black dashed lines) and the 95% confidence interval (gray dashed lines) of those estimated fractions in the corresponding figures.

To assess whether the modulation index was dominated by slow changes across many minutes during the recording, we calculated a pairwise modulation index between each high arousal trial and all low arousal trials in an epifluorescence imaging

session. We then compared the mean of these modulation indices for pairs of trials that were 0-5 min apart and for pairs that were 15-20 min apart.

Arousal modulation during the stationary state

The mouse was considered to be stationary during a given trial if, from 1 s before and 2 s after onset of visual stimulation, its movement speed didn't exceed 1.55 cm/s at any moment (i.e., in any frame, with sampling at 15.5 Hz) and the total movement was no more than 0.5 cm, the minimum step size of our rotary encoder. 1.55 cm/s was the minimum unit of running speed during a given frame, and 0.5 cm of movement is equivalent to movement at this minimal speed for 0.33 s. This criterion ensured that trials with occasional posture adjustments would still be considered as stationary trials. For analyses of arousal-dependent modulation index during stationary trials, we used the same pupil-based definition of low versus high arousal trials as above, but we now only included trials that met the additional criterion reflecting the stationary state. Across the 8 FOV from 4 mice used for assessing arousal modulation during the stationary state, no single stimulus direction had fewer than 3 trials at either the low or high arousal state, and no 3 adjacent directions had fewer than 11 trials in total at either the low or high arousal state. On average, 13.3 ± 1.7 (mean \pm SEM) trials were included as low arousal trials, and 12.8 ± 2.5 trials were included as high arousal trials, for each stimulus direction at the intermediate spatial frequency.

Trial matching

To test whether differences in position or motion of the pupil in high versus low arousal trials contributed to the effect of arousal on response amplitude, we calculated the modulation index in the subsets of trials that were matched either for position of the pupil along the dorsal-ventral axis (Y position, in a.u.), or for the amount of pupil motion along the nasal-temporal axis (horizontal motion, or the standard deviation of the time course of X displacement), from 1 s before stimulus onset until the end of stimulus presentation for each trial. We randomly selected a high arousal trial and matched it with the low arousal trial that was most similar to it in terms of position or amount of motion (sampling without replacement). The difference in position between a high and low arousal trial had to be below 2 a.u. (estimated to correspond to ~ 1 degree of pupil rotation) and the difference in standard deviation estimates of motion had to be less than 0.5 a.u. If no low arousal trial fulfilled these criteria, the high arousal trial was not considered. We continued this procedure until all high arousal trials with a suitable match were found. We then calculated the modulation index using the set of matched high and low arousal trials. The matching procedure was repeated 100 times, randomizing the order in which high arousal trials were chosen for matching. We report the average modulation index (and average estimate of standard error) across 100 repetitions of the matching procedure.

To estimate the overall degree of dissimilarity between unmatched distributions of pupil location during high versus low arousal (Figure S2C, right, and S2D, right), we used the Bhattacharyya distance [57]. This distance is defined, for discrete probability distributions, as $-\ln(BC(p, q))$, where $BC(p, q) = \sum_{i=1}^N \sqrt{p(i)q(i)}$. $p(i)$ and $q(i)$ are the area-normalized distribution probability in the i th bin of low and high arousal trials, respectively.

Estimation of retinotopic preferences in RGC boutons

Retinotopic tuning curve fitting

Two retinotopic tuning curves, which were independently fitted for each bouton, were established, respectively, for tuning along the azimuth and along the elevation axes. Both curves consisted of eight evenly spaced values, each consisting of the average response across trials for a given location in visual space of the oriented bar containing binarized spatiotemporal noise (see above). Tuning curves were approximated using a Gaussian function:

$$R(x) = R_1 e^{-\frac{(x-x_{pref})^2}{2\sigma^2}} + R_{off}$$

The $\Delta F/F$ response, $R(x)$ varied as a function of the retinotopic stimulus location, x . The maximum response, $R_1 + R_{off}$, was evoked at x_{pref} , the preferred retinotopic location. The standard deviation σ of the Gaussian was proportional to the receptive field size along this axis. To increase the number of points for fitting from 8 to 15, an interpolation method similar to the one used for direction tuning curves was implemented. As responses were very reliable and well fit, no bootstrapping method was implemented. Fitting was considered significant if 2 out of the 8 directions showed a significant response (see Subsection, 'Estimation of boutons with significant visual responses'), if the absolute correlation coefficient $\sqrt{r^2}$ exceeded 0.8, and if the fitted peak amplitude was confirmed to be positive or negative for non-suppressed and for suppressed boutons, respectively.

QUANTIFICATION AND STATISTICAL ANALYSES

Statistical tests were conducted using MATLAB and Prism. Non-parametric tests were used for comparing two independent groups (Mann-Whitney-Wilcoxon test), two related groups (Wilcoxon signed-rank test), and multiple independent groups (Kruskal-Wallis test with post hoc Dunn's multiple comparison test), multiple related groups (Friedman test with post hoc Dunn's multiple comparison test). To consider multiple factors and their interaction (for example, spatial frequency and mouse identity), a two-way or N-way

ANOVA test was used. To test whether the mean of a normal distribution is significantly different from 0, a t test was used. A Kolmogorov-Smirnov test was performed to compare cumulative distributions. $p < 0.05$ was considered significant. To consider not only whether differences are significant but also how large the differences are given the spread in the distributions, we computed the area under the curve (AUC) for the receiver operating characteristic (ROC) curve for each pair of modulation index distributions in the associated plot, with probability estimates derived from the logistic regression model. Additional details on sample sizes, statistical test, significant levels for each experiment can be found in figure legends, Results and Star Methods. All acquired data were included for analyses.